RESEARCH ARTICLE

Key Points:
- An ~11-Ma syneruptive volcanic debris flow was identified within the Xiyu Formation in the Pamir-West Kunlun foreland basin
- The Tashkorgan River was established before ~15 Ma, while the Yarkand River was developed after ~11 Ma
- No large-scale offset between the Pamir and the Tarim occurred after ~11 Ma

Miocene Volcaniclastic Sequence Within the Xiyu Formation from Source to Sink: Implications for Drainage Development and Tectonic Evolution in Eastern Pamir, NW Tibetan Plateau

Xiaochun Wei[1] [iD]**, Hongbo Zheng[2], Ping Wang[3], Ryuji Tada[4]** [iD]**, Peter D. Clift[5]** [iD]**, Fred Jourdan[6]** [iD]**, Chao Luo[3], and Hanlin Chen[7]** [iD]

[1]School of Earth Sciences and Engineering, Nanjing University, Nanjing, China, [2]Research Center for Earth System Science, Yunnan University, Kunming, China, [3]School of Geography Science, Nanjing Normal University, Nanjing, China, [4]Department of Earth and Planetary Science, University of Tokyo, Tokyo, Japan, [5]Department of Geology and Geophysics, Louisiana State University, Baton Rouge, LA, USA, [6]Western Australian Argon Isotope Facility, Department of Applied Geology and JdL Centre, Curtin University, Perth, WA, Australia, [7]School of Earth Sciences, Zhejiang University, Hangzhou, China

Abstract The formation of the Pamir salient and the Tashkorgan-Yarkand River is highly debated with the ages ranging from pre-Cenozoic to late Miocene. One approach to resolve these issues is to draw support from the sedimentary record in the surrounding basins. A volcaniclastic sequence, which divides into Lower and Upper Members, was identified in the southwestern Tarim Basin. The Lower Member was transported by dilute streamflows, which likely flowed during or soon after eruptions, while the Upper Member was formed by a syneruptive volcanic debris flow. Chronological, petrologic, and geochemical data consistently indicate that the sequence was derived from the Central Pamir at ~11 Ma. The ~11 Ma emplacement of the volcaniclastic sequence provides unique constraints for the evolution of the Tashkorgan-Yarkand River and the Pamir salient. Provenance data indicate a multistage evolutionary history of the Tashkorgan-Yarkand River. The paleo-Tashkorgan River was initially formed in the piedmont of the Pamir marginal range before ~15 Ma. This river cut back into the Tashkorgan region at ~15 Ma, after which it has eroded the Central Pamir by ~11 Ma. The N-S trending upper reaches of the Tashkorgan River and the Yarkand River were established after ~11 Ma. The emplacement of the volcanic debris flow, together with regional deformation evidence, indicates limited strike-slip motion between Pamir and the Tarim at least since ~11 Ma, which refutes hundreds of kilometers offset between the Pamir and the Tarim after this time and supports an earlier indention of the Pamir salient.

1. Introduction

The Pamir salient comprises the northwest part of the Tibetan Plateau and is a natural laboratory for studying the mechanisms and processes of collisional orogenic belts (Figure 1a; e.g., Burtman & Molnar, 1993; Kufner et al., 2016; Robinson et al., 2004; Schurr et al., 2014; Sippl et al., 2013; Sobel et al., 2013). However, when the strong arcuate Pamir salient was formed is still controversial. A set of models suggests a pre-Cenozoic antecedent arcuate Pamir salient (Chapman et al., 2017; Chen et al., 2018; Coutand et al., 2002). Another set of models suggests that the Pamir-Western Kunlun range formed a single, sublinear belt that lay along the southern margin of the Tajik-Tarim Basin in the early Cenozoic, ~300–380 km south of the present position (e.g., Burtman, 2000; Burtman & Molnar, 1993; Cowgill, 2010; Kufner et al., 2016; Rutte, Ratschbacher, Khan, et al., 2017; Rutte, Ratschbacher, Schneider, et al., 2017). Then, the Pamir has initially moved northward relative to the West Kunlun in the Eocene or early Miocene following the indention of Indian Plate afterward, gradually forming its strongly curved geometry today (e.g., Bosboom, Dupont-Nivet, Huang, et al., 2014; Burtman, 2000; Burtman & Molnar, 1993; Cao, Wang, et al., 2013; Cowgill, 2010; Sobel & Dumitru, 1997). Nevertheless, recent studies proposed that significant indention of the Pamir did not initiate until ~12–10 Ma when the northward moving Indian slab collided with the Asian lithospheric root (Kufner et al., 2016; Rutte, Ratschbacher, Khan, et al., 2017). Here the indention of the Pamir is defined by the northward displacement of the Pamir salient relative to the Western Kunlun and the Tarim, accommodated by
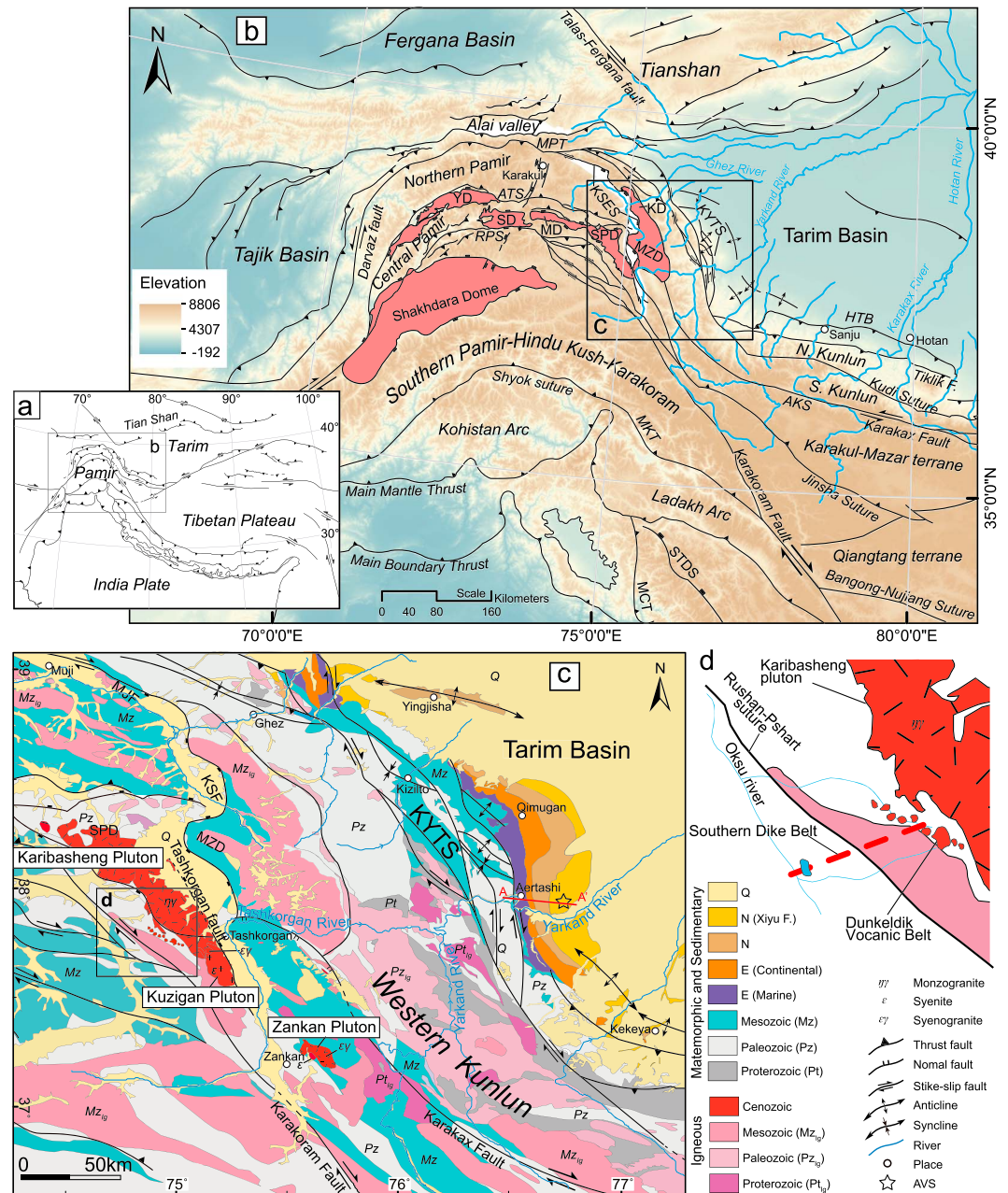
Figure 1. Simplified geologic map of study area and its surrounding regions. Major structures referred to in the text are indicated. (a) Tectonic map of the middle-western Tibetan Plateau and surrounding area, after Robinson et al. (2004). (b) Tectonic map of the northwestern Tibetan Plateau and its surrounding regions with major structures, based on Bakirov et al. (2001), Bande et al. (2015), Cowgill (2010), Robinson et al. (2004, 2007), and Stübner et al. (2013). The pink fills define the Cenozoic domes in Pamir. (c) Simplified geologic map of the study area, showing sedimentary, metamorphic, and igneous rocks and Quaternary sediments, as well as major structures, based on Cao, Bernet, et al. (2013), Chengdu Institute of Geology and Mineral Resources, C. A. of G. S. (1989), Cowgill (2010), Robinson et al. (2004, 2007), Schwab et al. (2004), Sobel et al. (2011), and our field work. The location of the volcaniclastic sequence is marked by the star. (d) Location of Dunkeldik volcanic field in the southeastern Pamir, after Hacker et al. (2005) and Schwab et al. (2004). MPT: Main Pamir Thrust, KSES: Kongur Shan Extensional System, KSF: Kongur Shan Fault, KYTS: Kashi Yecheng Transfer System, HBT: Hotan Thrust Belt, AKS: Anyimaqen-Kunlun Suture; TS: Tanymas Suture; MCT: Main Central Thrust; MJF: Muji Fault, RPS: Rushan-Pshart Suture; STDS: South Tibetan Detachment System, YD: Yazgulom Dome, SD: Sarez Dome, MD: Muskol Dome, SPD: Shatput Dome, MZD: Muztaghata Dome, KD: Kongur Shan Dome.

Table 1
Sample Information and Ages of the Dated Samples

No.	Samples no.	Latitude	Longitude	Sample description	Dated mineral	Age estimate (Ma; ±2σ)
Upper Member	AT12-HS-CM	37.988448	76.678976	Randomly selected trachyte block	Biotite	11.19 ± 0.03
					Sanidine	11.27 ± 0.03[xn]
	AT12-HS-1	37.988440	76.678336	Randomly selected phonolite block	Sanidine	11.07 ± 0.13
	AT12-04	37.988712	76.678896	Matrix of the Debris Flow Deposits	Sanidine	11.24 ± 0.04
Lower Member	AT10-34*	37.987346	76.675313	Tuffaceous sandstone	Biotite	10.94 ± 0.20
	AT10-35*	37.987320	76.675589	Tuffaceous sandstone	Biotite	11.49 ± 0.34

Note. Ar isotopic data corrected for blank, mass discrimination and radioactive decay are given in Data Sets S2–S5. An asterisk (*) mark after the Sample Number denotes the data published by Zheng et al. (2015a). [xn] indicate that the age is likely due to a xenocryst population (cf. discussion).

vertical-axis rotation of the flanks of the plateau via radial thrusting and/or deformation via conjugate strike-slip transfer fault systems (e.g., Bazhenov, 1993; Bosboom, Dupont-Nivet, Huang, et al., 2014; Cowgill, 2010; Sobel & Dumitru, 1997; Thomas et al., 1994).

Fluvial systems are sensitive to tectonism in orogenic belts (e.g., Clark et al., 2004). Analysis of fluvial system is critical for understanding tectonism. As the largest river system in Eastern Pamir region, the Tashkorgan-Yarkand River plays an important role in sourcing sediments from the Pamir-Western Kunlun range into the Tarim Basin (Figure 1b; e.g., Clift et al., 2017). However, the evolution of this river remains an open question. Sobel et al. (2011) proposed that the Tashkorgan River was an antecedent river considering the difficulty in achieving long-distance headward erosion perpendicular to large mountains. Using detrital zircon dating, Cao et al. (2014) inferred that the Yarkand River has been formed by mid-Miocene, while the Tashkorgan River has not reached the Tashkorgan region prior to the Pliocene. Recent studies, also based on provenance identification, proposed that Tashkorgan-Yarkand River was established after late Miocene (Blayney et al., 2016; Clift et al., 2017).

Sedimentary rocks preserved in the southwestern Tarim Basin provide important information on the history of fluvial evolution and tectonic deformation of Pamir-Western Kunlun range (e.g., Blayney et al., 2016; Cao et al., 2014, 2015; Sobel & Dumitru, 1997; Yin et al., 2002). A volcaniclastic sequence within the fluvial sedimentary rocks in the Pamir-West Kunlun foreland basin has long been overlooked, partly because of its similarity with the surrounding sandstone. Previously, Zheng et al. (2015a) reported the volcaniclastic sequence within the Xiyu Formation, which was dated at ~11 Ma, and constructed an accurate geochronological framework for the Cenozoic continental deposits in the southwestern Tarim Basin. However, those new ages caused controversy, particularly whether the sequence was deposited syneruptively or very recently afterward (Sun et al., 2015; Zheng et al., 2015b). Correct identification and dating of these specific volcaniclastic deposits is critically important as these data provide unique information on volcanic history, geochronological framework, fluvial evolution, and tectonics in Pamir-Western Kunlun region.

We have conducted comprehensive research on this sequence at Aertashi, which is termed as the Aertashi Volcaniclastic Sequence (AVS) in this contribution. Here we present detailed sedimentary, petrological, geochemical, and chronological results to demonstrate the source to sink processes of the volcaniclastic sequence and its geochronologic, geomorphological, and tectonic significance. Particularly noteworthy are the newly identified volcanic debris flow deposits within the sequence, which is interpreted as a fast moving syneruptive volcanic debris flow, likely transformed from an initial slope failure at the volcanic center during an eruption. The emplacement of the debris flow provides useful constraints on fluvial evolution and tectonics in Pamir-Western Kunlun region. Based on a review of provenance data, we suggest that the Tashkorgan-Yarkand River system has a multistage evolutionary history. Our results do not support a large-scale northward indention of the Pamir after ~11 Ma and tend to support an earlier formation of the arcuate Pamir salient.

2. Geological Setting

2.1. Tectonics and Topography

The Pamir-West Kunlun region constitutes the northeastern part of the western Tibetan Plateau (Figures 1a and 1b) and is the product of a long-term accretionary orogeny that consumed the Paleotethys and

Neotethys oceans in the Paleozoic to Mesozoic (e.g., Mattern & Schneider, 2000; Pan, 1996; Robinson et al., 2012; Xiao et al., 2002, 2003). Prior to the collision between the Asian Plate with Indian Plate in the early Cenozoic, five terranes, including the Kunlun terrane, the Karakul-Mazar terrane, the Central Pamir terrane, the Karakoram-Qiangtang terrane, and the Kohistan-Ladakh arc, were formed along, or accreted to, the southern margin of Asian Plate (Figure 1b; e.g., Schwab et al., 2004; Xiao et al., 2003). Long-term multiple accretionary orogeny induced significant continental growth in this region (e.g., Xiao et al., 2003).

Cenozoic orogenic rejuvenation following India-Eurasia continental collision has greatly impacted the geometry of the Pamir (e.g., Burtman & Molnar, 1993; Cowgill, 2010). The modern western, northern, and eastern margins of the range are defined by the Darvaz fault, Main Pamir Thrust (MPT), and Kashi-Yecheng Transfer System (KYTS), respectively (Figure 1b; Cowgill, 2010). Seismic and geophysical evidence demonstrates south dipping Asian lithosphere under the Pamir salient (e.g., Burtman & Molnar, 1993; Kufner et al., 2016; Sippl et al., 2013). A set of models suggests a pre-Cenozoic antecedent arcuate Pamir salient and predicts only tens of kilometers northward displacement of the Pamir salient as a result of the indention of the Indian Plate (e.g., Chapman et al., 2017; Chen et al., 2018; Coutand et al., 2002). Another set of models suggests that the Pamir-Western Kunlun range formed a single, sublinear belt that lay ~300–380 km south of the modern Alai valley in the early Cenozoic (e.g., Burtman, 2000; Burtman & Molnar, 1993; Cowgill, 2010; Kufner et al., 2016; Rutte, Ratschbacher, Khan, et al., 2017). Subsequently, the Northern Pamir has been displaced ~300 km northward relative to the Alai Valley, accommodated by overthrusting along the MPT or equivalent, older structures (e.g., Burtman, 2000; Burtman & Molnar, 1993; Cowgill, 2010). Two popular end-member kinematic models accommodating the large-scale northward indentation of the Pamir involve vertical-axis rotation of the flanks of the plateau via radial thrusting and deformation via conjugate strike-slip transfer fault systems (e.g., Bazhenov, 1993; Bosboom, Dupont-Nivet, Huang, et al., 2014; Cowgill, 2010; Sobel & Dumitru, 1997; Thomas et al., 1994). The KYTS, a fault system consisting of four parallel dextral strike slips, is proposed to have accommodated the separation of the Northern Pamir from the Western Kunlun by motion on the order of ~280 km on the eastern flank of the Pamir (Cowgill, 2010). In these large-scale Cenozoic indention models, the timing of separation of the Northern Pamir from the West Kunlun has been suggested to be either Eocene (e.g., Bosboom, Dupont-Nivet, Huang, et al., 2014; Burtman & Molnar, 1993; Cao, Wang, et al., 2013; Yin et al., 2002) or late Oligocene to early Miocene (e.g., Blayney et al., 2016; Burtman & Molnar, 1993; Cowgill, 2010; Sobel & Dumitru, 1997). Recently, it was argued that significant indention of the Pamir did not initiate until ~12–10 Ma (Kufner et al., 2016; Rutte, Ratschbacher, Khan, et al., 2017). Thermochronologic data and geomorphic observations suggest that northward indention of the Pamir relative to the Tarim Block has been inactive since at least 3–5 Ma (Sobel et al., 2011).

One of distinctions between the Pamir and the Tibetan Plateau is that the former contains a series of domes that have exhumed deeply buried amphibolite-facies metamorphic rocks (Figures 1b and 1c; e.g., Hacker et al., 2017; Robinson et al., 2007; Schmidt et al., 2011; Stübner et al., 2013). The doubly vergent Shakhdara dome of the Southern Pamir and the Yazgulem, Sarez, and Muskol-Shatput domes of the Central Pamir were formed by approximately N-S extensional doming with footwall exhumation along dome-bounding normal-sense shear zones at ~23–20 Ma, following crustal thickening and heating in the Eocene and Oligocene (Figures 1b and 1c; e.g., Rutte, Ratschbacher, Khan, et al., 2017; Stearns et al., 2013; Stübner et al., 2013). In the east part of the Pamir, the Kongur Shan Extensional System (KSES), consisting of a series of normal faults (Muji Fault, Kongur Shan Fault, Tahman Fault, and Tashkorgan Fault), separates the Eastern Pamir domes to the east (Figures 1b and 1c; Robinson et al., 2004). The Muztaghata dome has been suggested to be the eastward continuation of the Muskol-Shatput dome of the Central Pamir and has started doming in the late Miocene (Cao, Bernet, et al., 2013; Robinson et al., 2007) or early Miocene (Rutte, Ratschbacher, Khan, et al., 2017). The Kongur Shan dome has been suggested to be exhumed mostly by the top-to-W Kongur Shan normal fault (Robinson et al., 2004; Rutte, Ratschbacher, Khan, et al., 2017). The initial extension of the KSES has been assigned as ~8–7 Ma (Robinson et al., 2004; Thiede et al., 2013) or ~6–5 Ma (Cao, Bernet, et al., 2013; Robinson et al., 2004; Thiede et al., 2013) based on intermediate-low-T thermochronologic data. Recently, Rutte, Ratschbacher, Khan, et al. (2017) reinterpreted the monazite Th-Pb ages from the Eastern Pamir domes and proposed that the timing of onset of dip slip along the extensional system may have initiated ≥10 Ma.

The eastern flank of the Pamir is truncated by several deep valleys that are heavily incised by basinward flowing rivers, the largest of which is the Tashkorgan-Yarkand River (Figure 1b). This river contains two major

branches, the Yarkand River and the Tashkorgan River. The Yarkand River drains the Southern Pamir, the Karakul-Mazar, and the Kunlun terranes from south to north, while the Tashkorgan River drains the Southern Pamir, the Eastern Pamir domes, and the Kunlun terrane from west to east (Figure 1b). Provenance study of Cenozoic sedimentary rocks deposited in the Aertashi section in the Tarim Basin, which likely record the drainage evolution of the paleo-Tashkorgan-Yarkand River, suggested that the provenance at the Aertashi area was dominated by the Kunlun terrane during the Eocene to ~15 Ma and with a greater contribution from the Northern Pamir since ~15 Ma (Blayney et al., 2016). The evolutionary history of the modern Tashkorgan-Yarkand River, which transports significant volumes of sediment eroded from the Southern Pamir, is still under debate (e.g., Blayney et al., 2016; Cao et al., 2014; Clift et al., 2017).

2.2. ~11 Ma Igneous Rocks

A series of ~11-Ma alkaline rocks along the KSES (e.g., Ducea et al., 2003; Jiang et al., 2012; Kooijman et al., 2017; Shaffer et al., 2017) are included in the scope of this study (Figures 1c and 1d). The alkaline rocks, which are found in three plutons (Karibasheng, Kuzigan, and Zankan) called the Tashkorgan plutons along the Tashkorgan valley (Jiang et al., 2012; Ke et al., 2006), as well as in a volcanic-subvolcanic complex called the Dunkeldik volcanic complex, are the youngest igneous rocks in the Pamir (Figure 1c; Lutkov et al., 2005). The Karibasheng pluton consists of monzogranite, whereas the Kuzigan and Zankan plutons are intrusive bodies composed of syenite and syenogranite (Jiang et al., 2012; Ke et al., 2006). The Dunkeldik volcanic complex, located in the Dunkeldik valley (Figures 1c and 1d), consists of a series of alkaline volcanic-hypabyssal complex, including a subvolcanic massif, two dike belts, and nine diatremes, which shows both intrusive and volcanic facies (explosive breccias and tuff dikes; Dmitriev, 1976; Lutkov et al., 2005). The compositions within the complex range from ultrapotassic alkaline gabbro and basalts (fergusite and fergusite porphyry) to various syenitoids (leucitic and sanidine pyroxene syenite porphyry, alkalic syenite, leucitic tinguaite, pseudoleucitic tinguaite, trachyte, quartz syenite, and trachyrhyolite) and carbonatite (Dmitriev, 1976; Lutkov et al., 2005).

2.3. Cenozoic Stratigraphy

This study focuses on the area around Aertashi, which is located in the southwestern margin of the Tarim Basin and on the northern margin of the Pamir-West Kunlun range (Figure 1). Thick Cenozoic sequences have accumulated in the Pamir-West Kunlun foreland basin (Jia, 1997). They are well exposed and normally eastward dipping due to tectonic deformation. The Paleocene and lower Eocene are dominated by marine strata as a result of the intrusions of the Paratethys, a vast shallow epicontinental sea extended from Europe to the Tarim Basin during Cretaceous and Paleogene (e.g., Bosboom et al., 2011; Bosboom et al., 2014a, 2014b). Biostratigraphic, lithostratigraphic, and magnetostratigraphic evidence indicate the final regression of the Paratethys sea from the SW Tarim Basin was at ~41 Ma (Bosboom et al., 2014a; Zheng et al., 2015a).

Continental sedimentation immediately followed the marine regression and reached a thickness >10 km (Jia, 1997). The upper Eocene and Oligocene are dominated by reddish fine-grained sandstone interbedded with mudstone, which are interpreted as delta, playa lake, meandering, and braided river facies (Figure 2). The lower Miocene sequences are of distal alluvial and fluvial facies containing cobble conglomerate, brown medium-grained sandstone interbedded with siltstone (Figure 2).

The Xiyu Formation forms the uppermost part of the section, the base of which is marked by an abrupt change in lithology from reddish-brown siltstone and sandstone below to ~20 m thick massive, gray, gravelly medium-grained sandstone (Figure 2). The section then coarsens up into massive cobble-boulder conglomerate that is at least 3 km thick. Most of the gravel clasts in the conglomerates are rounded to subrounded, clast supported but poorly sorted, with sizes ranging from several centimeters to as large as 1 m. Almost no intercalations except very rare small lenses of coarse sandstone are present throughout the whole formation. The Xiyu Formation, or the so-called Xiyu Conglomerate, is typical of proximal alluvial fan deposits derived from unroofed mountain belts.

The AVS was identified in the Xiyu Formation at the Aertashi section. It was divided into the Lower and Upper Members based on lithological characters. Hereinafter, we first clarify the important terms and methods used in this study and present detailed sedimentary, petrological, geochemical, and chronologic information of the sequence.
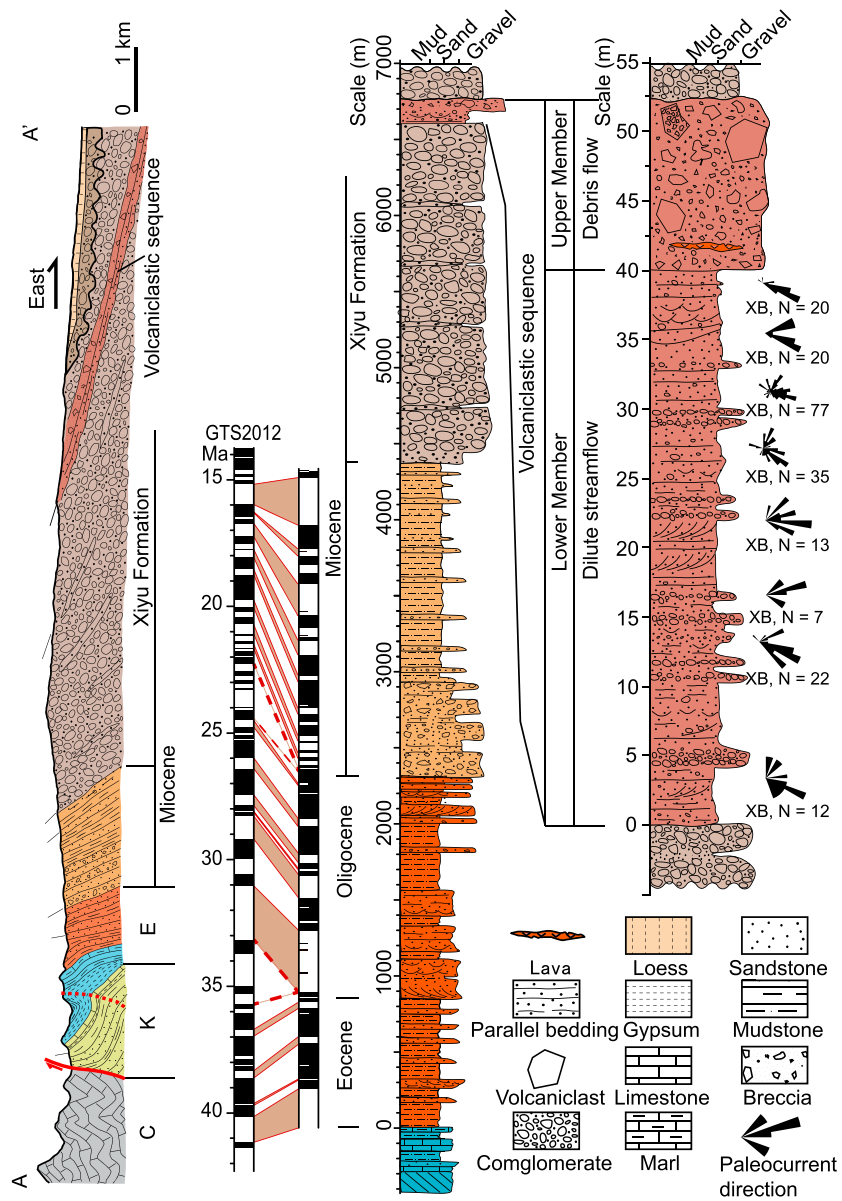
Figure 2. Stratigraphic and magnetostratigraphic section of the Aertashi section including the volcaniclastic sequence. The positions of the Aertashi transect are indicated in Figure 1c. The magnetostratigraphic is from Zheng et al. (2015a). See text for details. XB: Cross bedding.

3. Terminology and Methodology

3.1. Terminology

Volcano-hydrologic processes dominate the interdisciplinary areas between volcanology and sedimentology. There is still no unanimous terminology scheme for the products of these processes (e.g., Fisher & Schmincke, 1984; McPhie et al., 1993; Waitt, 2007; White & Houghton, 2007). In this study, for simplicity the general term "volcaniclastic" is used to include "all clastic volcanic materials formed by any process of fragmentation, dispersed by any kind of transporting agent, deposited in any environment or mixed in any significant portion with non-volcanic fragments" (Fisher, 1961; Fisher & Schmincke, 1984). We term all of the sand-sized rocks dominated by volcaniclastic compositions within the Lower Member as tuffaceous sandstone without distinguishing the tuff and the tuffaceous sandstone, which depends on the proportions of volcanic clasts and nonvolcanic clasts (Fisher & Schmincke, 1984).

The terms debris avalanche, debris flow, and landslide in this study refer to those of subaerial volcanic processes, unless otherwise specified.

3.2. Methodology

This study interprets the transport processes of the volcaniclastic sequence within the Xiyu Formation and its implications for drainage development and tectonic deformation. To determine the nature and provenance of the sequence is the key to our study. Lithostratigraphic observation and petrologic study are critical for the identification of the volcanic origin clasts. Paleocurrent analysis, as well as major and trace element analyses, inform on the nature and provenance of the sequence. $^{40}Ar/^{39}Ar$ chronological measurements provide the most important age constraints for the regional stratigraphic framework and help determine provenance.

Detailed field lithostratigraphic mapping and paleocurrent analysis was first carried out for the studied sequence, which provided the basis for further laboratory research. Cross bedding within the tuffaceous sandstone was measured for paleocurrent analysis.

To better understand the mineral assemblage and textures of the volcaniclastic rocks, we carried out a petrologic study. Samples of volcaniclastic rocks from the Lower Member, as well as matrix and lithic blocks from the Upper Member, were selected for thin-section preparation.

For major element analyses, samples were crushed to 200 mesh and fused into glass beads. Analyses were determined by X-ray fluorescence spectrometry at the State Key Laboratory for Mineral Deposits Research, Nanjing University. Whole-rock powders for trace elements analysis were dissolved in Teflon beakers by HNO_3 + HF solution and heated at about 160 °C for 48 hr. Trace element concentrations were determined using a Finnigan Element II inductively coupled plasma mass spectrometry also at Nanjing University.

Three samples, from the matrix, trachyte, and phonolite blocks of the Upper Member of the deposits, were randomly selected for $^{40}Ar/^{39}Ar$ dating. Biotite and/or sanidine were separated using a Frantz magnetic separator and then carefully handpicked under a binocular microscope. For igneous samples, a standard step-heating approach on single to tens of mineral grains is normally used to generate age spectra and eventually obtain plateau ages (McDougall & Harrison, 1999). However, such an approach is not used for pyroclastic rocks because they could include a mixture of juvenile crystals, as well as crystals inherited from previous eruptions. Therefore, we analyzed a population of 10–15 crystals by single-grain total fusion analysis for each sample at the Western Australian Argon Isotope Facility at Curtin University. We looked for age convergence of the youngest population with a minimum of four grains yielding an indistinguishable age as the best estimate of the eruption age. This procedure is similar to the approach used for individual ID-TIMS U-Pb zircon age to calculate a magmatic age. We applied the single-grain total fusion method to all samples to keep methodological consistency. Detailed analytical methods are described in the supporting information and references therein (Jourdan et al., 2014; Jourdan & Renne, 2007; Koppers, 2002; Phillips & Matchan, 2013; Renne et al., 2011).

4. Results

4.1. Lithostratigraphy

Here we focus on the field observation of the AVS. Detailed interpretation of the processes of deposition will be discussed together with other evidence in section 5.3.

4.1.1. The Lower Member

The Lower Member is usually ~40-m thick but reaches ~60 m in some locations (Figures 2 and 3a). The base of this member is defined by the first occurrence of thick-bedded gravelly tuffaceous sandstone. This member is dominated by dark gray, thick-bedded, massive tuffaceous sandstone (Figure 3b), with or without occasional, well-rounded gravel clasts, intercalated with 0.1 to 3-m thick beds of well-rounded, pebble to cobble, polymictic conglomerates that are similar to those found within the Xiyu Conglomerate (Figure 3d). Cross bedding and parallel bedding are developed in the tuffaceous sandstones (Figure 3c). The presence of cross bedding and interbedded conglomerates in the tuffaceous sandstone could give the misleading impression that they are nonvolcanic fluvial deposits. However, hand specimen observation indicates that these are likely volcaniclastic rocks composed of abundant pyroxene, feldspar, and quite unusual mineral grains with form of cubic icositetrahedron (microscopically indentified as pseudoleucite; see section 4.2), which strongly differ from the typical gray-yellowish, quartz-dominated sandstone lenses composed mainly of quartz and
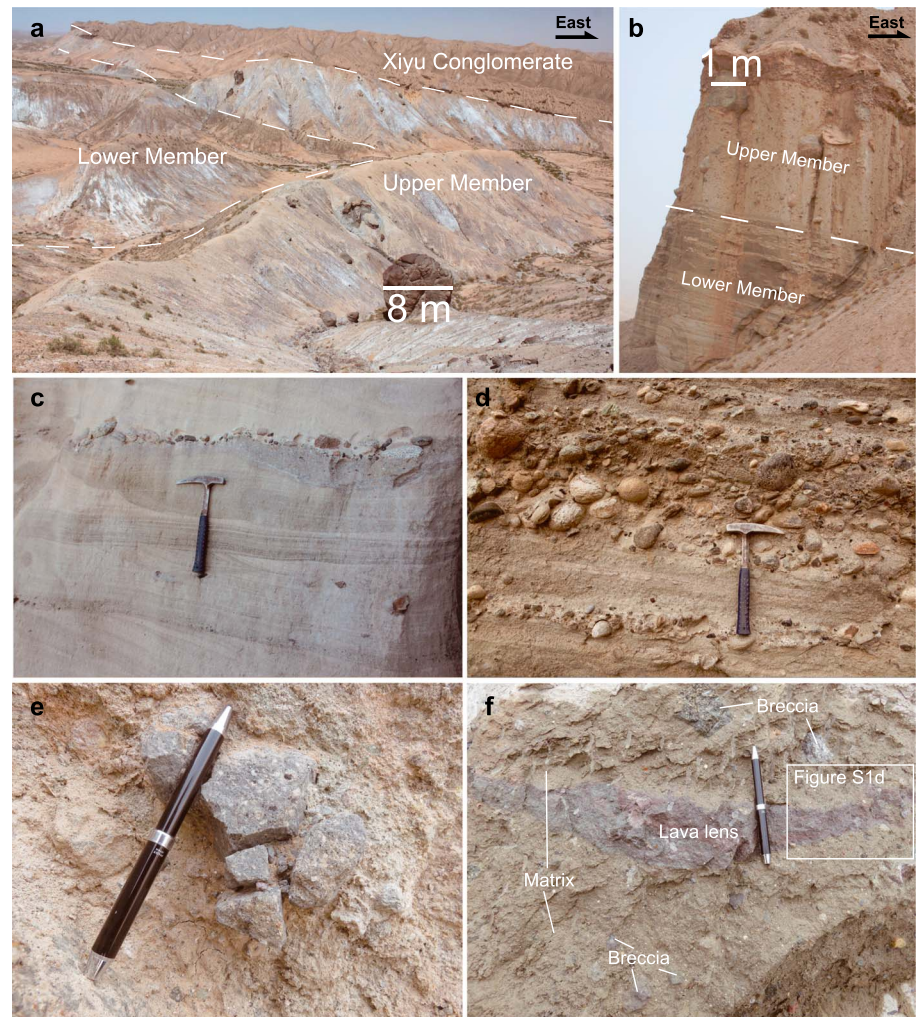
Figure 3. Field photos of the volcaniclastic sequence. Views in figures a–d are toward the north. The top and bottom boundaries of the Upper Member are indicated by dashed lines. (a) Panoramic view of the volcaniclastic sequence intercalated in the Xiyu Conglomerate. (b) Nearby view of the volcaniclastic sequence. (c) Typical tuffaceous sandstone of the Lower Member showing cross bedding and sporadic gravels. (d) Conglomerate layers intercalated within the Lower Member. (e) Rock domains of trachyte separated by matrix. (f) Lens of lava with plastic-flow-like shape, with a close-up photo shown in Figure S1d.

feldspar within the Xiyu Formation. Conglomerate layers are both matrix to clast supported and typically have scoured bases and show normal grading (Figure 3d). Gravel clasts of sedimentary (e.g., siltstone and chert), metamorphic (e.g., schist and gneiss), and igneous (e.g., dacite, granite, and syenite) origins are present. The dominance of tuffaceous clasts and the presence of cross bedding and parallel bedding of the Lower Member deposits match the characteristics of deposits formed by dilute streamflow derived from volcanic zones (e.g., Scott, 1988; Smith, 1986, 1991).

Paleocurrent measurement on the cross bedding of the Lower Member indicates that the sediments were derived from the west (Figure 2).

4.1.2. The Upper Member

The Upper Member conformably overlies but does not erode into tuffaceous sandstones of the Lower Member. The top of the Upper Member exhibits scour-and-fill structures and is overlain by massive polymictic conglomerates (Figures 3a and 3b). The thickness of this member ranges from several meters to ~30 m (Figures 2 and 3a). The deposits are massive, poorly sorted, and matrix supported, with particles ranging from clay to boulder size (Figures 3b and S1a). Rock fragments are dominated by angular to subangular volcanic rocks, including lava (trachyte, phonolite, and pseudoleucitite), agglomerate lava, volcanic breccia, and tuff.

AGU
100
ADVANCING EARTH
AND SPACE SCIENCE

Tectonics

10.1029/2018TC005008

Minor nonvolcanic angular rock fragments including schist, migmatite, syenite porphyry boulders, and rounded pebble-cobble-sized gravels, resembling those seen within the Xiyu Conglomerate, are present locally. Some megaclasts >1 m and up to ~8 m across are scattered in the deposits (Figures 3a and S1c). Jigsaw cracks are cracks characterized by irregular joint patterns within rock fragments (Smith & Lowe, 1991; Ui et al., 2000; Yarnold & Lombard, 1989). They have been observed in both volcanic and schist blocks (Figures S1b and S1c). Domains of clasts, within which clasts are monolithologic and separated by matrix, were present in some breccia (Figure 3e). We also observed lenses or belts of lava with plastic flow-like shapes and/or red oxidation edges (Figures 3f, S1d, S1e, and S1f). The matrix of this member is dominated by fine clasts (see next section).

The poor sorting and dominance of volcanic materials and the presence of jigsaw-fractured clasts and lava lenses/belts demonstrate that the Upper Member is deposited by a volcanic debris flow (e.g., Scott et al., 2001; Smith & Lowe, 1991; Ui et al., 2000). Detailed analysis of the depositional process of the flow will be discussed in section 5.3.

4.2. Petrography

Petrographic observations are focused on the volcanic rocks within the deposits. Characteristics of typical petrofacies are described below.

4.2.1. The Lower Member

Tuffaceous sandstones of the Lower Member mainly comprise lithic fragments, crystal fragments, and vitric fragments, up to 1.5 mm across (Figures 4a and S2a). Lithic fragments consist mainly of porphyritic clasts of pseudoleucitite, phonolite, trachyte dominated by phenocrysts of pseudoleucite, clinopyroxene, and sanidine, in a variably devitrified, black or brown, glassy groundmass (Figures 4a and S2a). Crystal fragments are dominated by pseudoleucite, sanidine, clinopyroxene, with minor biotite and muscovite, rare calcite, and quartz. Pseudoleucite, sanidine, and clinopyroxene grains commonly occur as subhedral crystals or angular broken fragments. Many crystal fragments are partially to wholly enclosed in glass. Glass injection into mineral fractures is observed, indicating that the minerals were broken during eruption. Minor biotite grains occur as elongate lamellae and are generally deformed adjacent to other clasts. Apatite and titanite are typical accessory minerals. Lithic and crystal fragments exhibit the same mineral assemblages as seen in the volcanic blocks within the Upper Member (see section 4.2.2.). Vitric fragments dominantly consist of blocky shards (Figures 4b and S2b). Bubble-wall shards have not been observed. Sparse rounded or irregular holes are observed in some glass shards and in the groundmass of lithic fragments; however, it is hard to determine whether these holes were formed by eruptive vesiculation or posteruptive alteration or abrasion of minerals such as pseudoleucite. Most of the glass, including glass in the groundmass of lithic fragments, glass coatings of fragments, and vitric fragments, is variably altered to brown or black zeolites and clay minerals. Authigenic zeolites and calcites act as cements.

4.2.2. The Upper Member

4.2.2.1. Lava Lenses

Samples of lava lenses/belts in the Upper Member show porphyritic texture and glassy groundmass (Figures 4c and S2c). Phenocrystic phases are sanidine and clinopyroxene, consisting ~20% by volume of the rocks. Sanidine phenocrysts are subhedral to anhedral elongate laths, less than 2 mm in length. Some crystals exhibit oscillatory zoning and/or contain inclusions of clinopyroxene. Simple contact twins are common in sanidine. Clinopyroxene phenocrysts are subhedral to euhedral and up to 2 mm across. Irregular or subparallel fractures can be observed in phenocrysts. Fragments of phenocrysts, which likely be formed by explosion during movement of lava, are common in phenocrystic phases. The groundmass of the lava is composed of dark glass, with very fine oxides dispersed. Typical accessory minerals are titanite and iron-titanium oxides.

4.2.2.2. Trachyte Blocks

Trachyte blocks show porphyritic or porphyaceous texture (Figures 4d and S2d). Phenocrystic phases consist ~10–35% by volume of the rocks and include sanidine, clinopyroxene, and minor plagioclase. Minor quartz phenocrysts can be observed in some samples. Sanidine phenocrysts in trachyte blocks also exhibit subhedral to anhedral elongate laths and oscillatory zoning and/or inclusions of clinopyroxene, and simple contact twins. They have larger sizes than those with lava lenses, with most of them less than 10 mm. Rare blocks contain sanidine phenocrysts up to 6-cm long. Clinopyroxene phenocrysts, including diopside, and minor
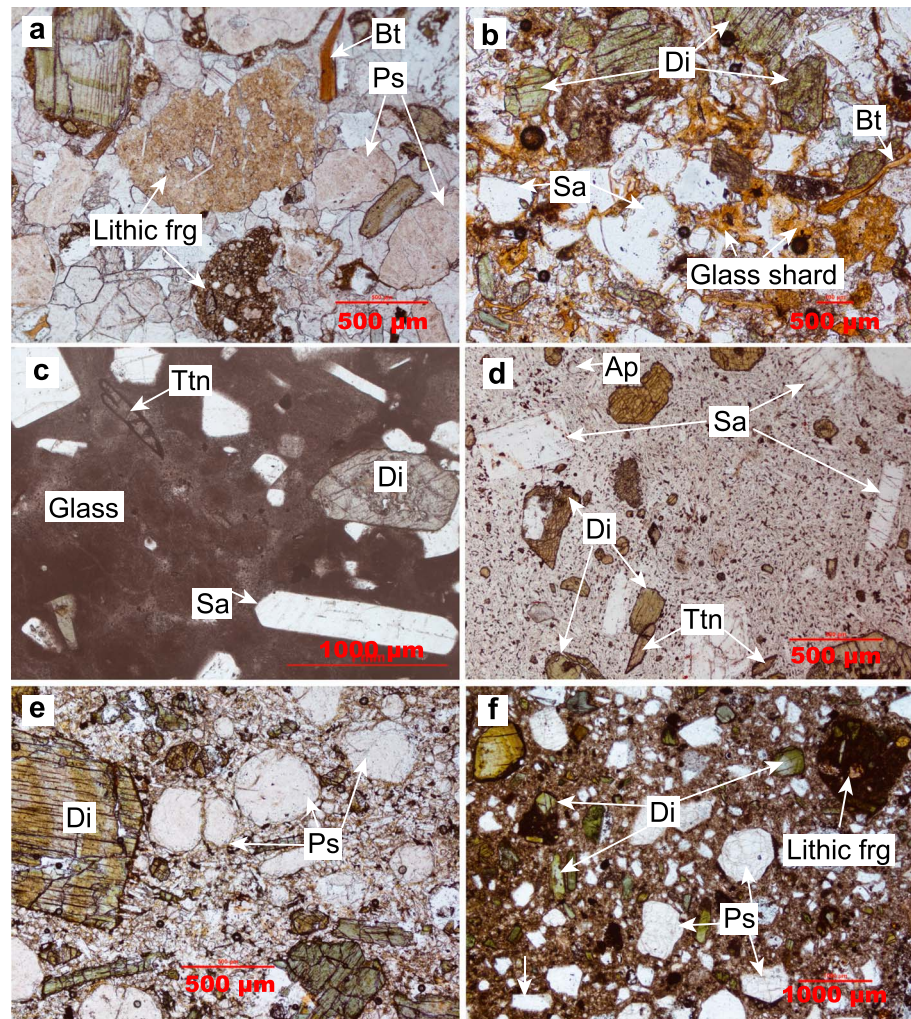
Figure 4. Thin section images in Plane Polarizer (PPL) of the AVS. The corresponding images in Crossed Polarizer (XPL) are showed in Figure S2. (a) Sample from lava lenses showing phenocrysts of clinopyroxene and tabular laths of sanidine within a glassy groundmass. (b) Sample from trachyte blocks showing porphyritic or porphyaceous texture. Phenocrystic phases mainly include sanidine and clinopyroxene. (c) Sample from phonolite blocks showing pseudoleucite, clinopyroxene, and minor tabular laths of sanidine within a microphenocrystic groundmass. (d) Sample from coarse-grained ash matrix within the Upper Member, with lithic fragments and crystal fragments of pseudoleucite, clinopyroxene, and sanidine. (e and f) Typical tuffaceous sandstone of the Lower Member, showing lithic fragments, crystal fragments, and glass shards. Ap: Apatite, Sa: Sanidine, Di: Diopside, Ttn: Titanite, Ps: Pseudoleucite, Lithic Frg: lithic fragment, Bt: Biotite, Cal: Calcite.

aegirine-augite, are subhedral to euhedral and up to 2 mm across. Diopside phenocrysts often have oxide inclusions and exhibit zoning, with color greening on the edges. Aegirine-augite is in the form of green, pleochroic crystals that are usually smaller than the diopside. Aegrine generally occurs as little dark green crystals coating diopside phenocrysts or dispersed in the groundmass. Irregular or subparallel fractures are common in phenocrysts. The groundmass of the trachyte blocks has a trachytic or subtrachytic texture and is dominated by fine-grained (<0.2 mm) sanidine and glass, with minor crystalline clinopyroxene, and oxides. Typical accessory minerals include apatite, titanite, rutile, and rare iron-titanium oxides and biotite. Minor crystalline calcite is dispersed in the groundmass and is present as veins along fractures within phenocrysts.

4.2.2.3. Pseudoleucite Phonolite Blocks

Phonolite blocks are porphyritic volcanic rocks dominated by phenocrysts of pseudoleucite (~5–60 vol%), clinopyroxene (~15–35 vol%), and tabular laths of sanidine (~5–60 vol%) within a microphenocrystic groundmass (Figures 4e and S2e). Pseudoleucite phenocrysts are subhedral to euhedral crystals, up to 8 mm in size,
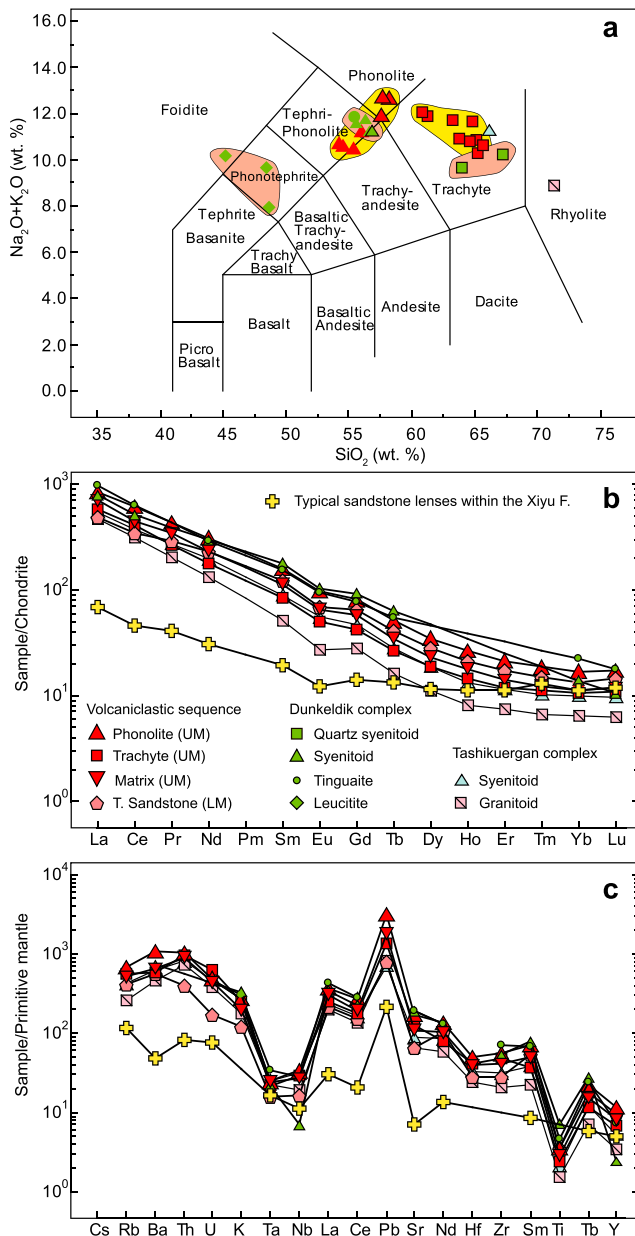
Figure 5. Geochemical data of AVS, Dunkeldik volcanic complex, and typical nonvolcanic fluvial sandstone with in the Xiyu Formation. Data of the Dunkeldik volcanic complex and the Tashkorgan complexes are average data from Lutkov et al. (2005) and Jiang et al. (2012), respectively. Figure legend is in (b). The data points with LOI > 2.5% are indicated by symbols without borders. (a) Total alkalis versus SiO_2. (b) Chondrite normalized REE patterns. (c) Primitive mantle normalized trace element patterns. Chondrite and primitive mantle values are from Boynton (1984) and McDonough et al. (1992), respectively. UM: Upper Member; LM: Lower Member.

and have typical cubic crystalline form. Most pseudoleucite crystals are analcite with leucite pseudomorphs showing rough surfaces and fractures (Figures 4e and S2e). The pseudoleucite conforms to the characteristics of secondary analcime that formed by an ion-exchange and hydration process from primary leucite (Putnis et al., 1994). Clinopyroxene and sanidine in phonolite show similar characteristics compared to those in the above mentioned trachyte. Accessory apatite and titanite are common. The groundmass is dominated by microphenocrysts of leucite/pseudoleucite, sanidine, with minor sparse brown glass and clinopyroxene. Minor calcite appears as crystals dispersed in the groundmass.

4.2.2.4. Matrix of Debris Flow Deposits

The matrix of the debris flow deposits is composed of relative fine-grained components and occupies variable proportions within the Upper Member. Petrologic observation of the matrix is critical to determine the mineralogical composition and physical property of the original flow.

The matrix of the Upper Member is poorly sorted, with grains ranging from volcanic ash to lapilli. As seen in the blocks in the debris flow, lapilli are dominated by angular to subangular dark to red volcanic rocks of trachyte and phonolite.

The coarse ash matrix of the Upper Member is composed of crystal fragments, lithic fragments, and interstitial materials (Figures 4f and S2f). Crystal fragments are dominated by angular broken fragments and euhedral single grains of sanidine, pseudoleucite, and clinopyroxene. We also observe minor plagioclase, opaque oxide, quartz, and rare biotite. Typical accessory minerals include apatite and titanite. Crystal fragments within the matrix show the same mineral assemblages as seen in the volcanic blocks. Lithic fragments are dominated by porphyritic or microlitic clasts of trachyte and phonolite, showing subrounded to angular shapes. Porphyritic fragments consist mainly of phenocrysts of clinopyroxene, sanidine, and pseudoleucite, in a trachytic sanidine-dominated or phonolitic glass-dominated groundmass. The glassy groundmass is partially or completely altered to black, brown, or microlitic opaque-dominated groundmass. Some lithic fragments have trachytic or subtrachytic textures, similar to the groundmass of the trachyte blocks. Minor schist fragments can also be observed.

Interstitial materials consist mainly of extremely fine crystal fragments, glass shards, and authigenic cements filling pores between coarse-grained ash clasts (Figures 4f and S2f). The composition of the microcrystal fragments is similar to the coarse crystal fragments. Glassy materials are variably devitrified and altered to zeolites, as well as minor clay minerals.

The above observations confirm that the debris flow deposits are of volcaniclastic origin.

4.3. Geochemistry

Major element data indicate that the trachyte blocks are intermediate to slightly acidic in composition, with SiO_2 contents of 60.9–65.74 wt.% (Data Set S1 and Figure 5a). These rocks are generally peraluminous and belong to the shoshonitic series. They have high alkali (K_2O + Na_2O = 10.3–12.0 wt.%), high K_2O contents (6.7–8.6 wt.%), with K_2O/Na_2O ratios ranging 1.6–2.5. Another obvious character of these rocks is their enrichment in large ion lithophile elements (LILE; e.g., Ba = 3,750–5,480 ppm, average = 4,162 ppm; Sr = 2,190–3,310 ppm, average = 2,675 ppm), and the rare-earth elements (REE; 623–760 ppm, average = 693 ppm), especially the light REE (La/Yb = 70–120; Figure 5b). On the other hand, they are relatively depleted in high field
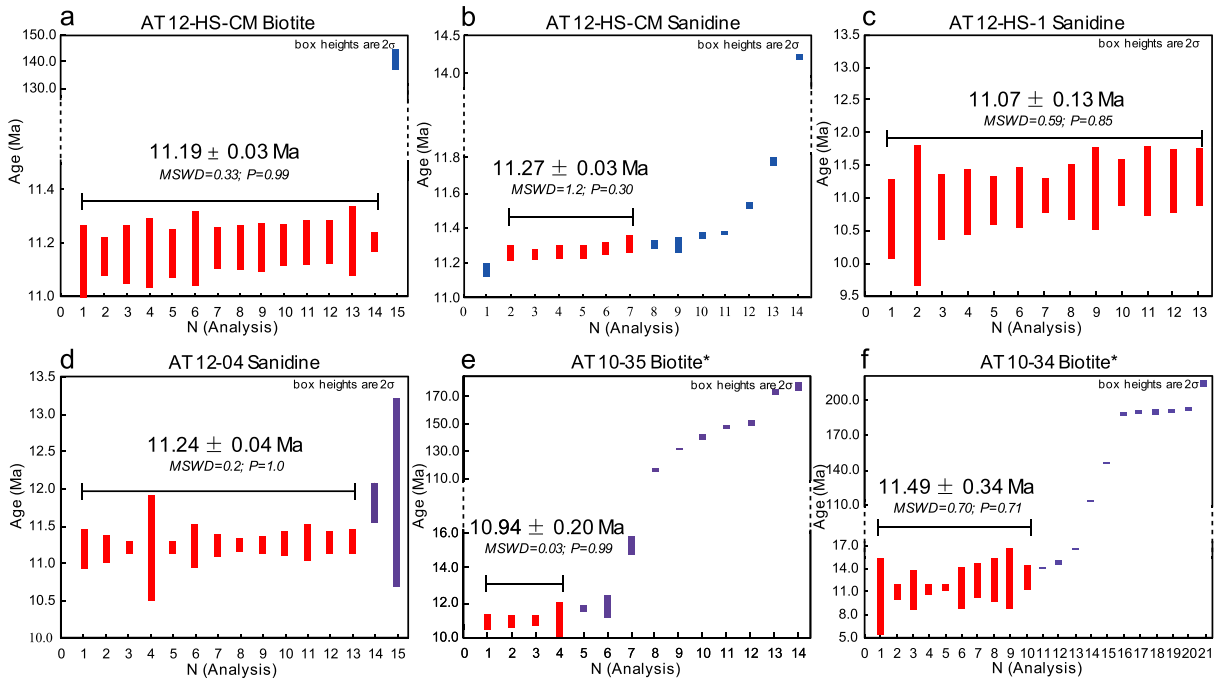
Figure 6. Total fusion $^{40}Ar/^{39}Ar$ age plots. Weighted mean ages were calculated using the youngest concordant crystal populations. Data published in Zheng et al. (2015a) is marked by *. (a) The 14 youngest biotite crystals from sample AT12-HS-CM yielding a weighted mean age of 11.19 ± 0.03 Ma (MSWD = 0.33, P = 0.99). (b) The six youngest sanidine crystals from sample AT12-HS-CM yielding a weighted mean age of 11.27 ± 0.03 Ma (MSWD = 1.2, P = 0.30). (c) All 13 sanidine crystals from sample AT12-HS-1 yielded a weighted mean age of 11.07 ± 0.13 Ma (MSWD = 0,59, P = 0.85). (d) Thirteen sanidine crystals from sample AT12-04 give a weighted mean age of 11.24 ± 0.04 Ma (MSWD = 0, 1, P = 1.0). (e) The four youngest biotite grains from sample AT10-34 give a weighted mean age of 10.94 ± 0.20 Ma (MSWD = 0.03, P = 0.99). (f) Ten youngest grains of AT10-35 yielded a weighted mean age of 11.49 ± 0.34 Ma (MSWD = 0.70, P = 0.71). Sample information and ages of the dated samples are integrated in Table 1.

strength elements, such as Nb, Ta, Hf, and Ti (Figure 5c). The samples from the phonolite blocks show higher Loss On Ignition (LOI; 1.2–5.4 wt.%) than those from the trachyte (0.2–0.8 wt.%; Data Set S1 and Figure 5a), likely due to the presence of hydrous pseudoleucitite. Phonolite samples with LOI <2.5 wt.% show lower SiO_2 (54.3–58.3 wt.%) but higher alkali ($K_2O + Na_2O$ = 11.9–12.7 wt.%), K_2O contents (9.0–9.2 wt.%), MgO contents (2.4–3.0 wt.%), and K_2O/Na_2O ratios (2.4–3.3) (Data Set S1). Phonolite samples are part of the ultrapotassic series and show higher contents of LILEs (e.g., Ba = 6,360–10,000 ppm, average = 7,588 ppm; Sr = 3,230–4,190 ppm, average = 3,575 ppm), the REE (875–1,166 ppm, average = 1,078 ppm) compared to the trachyte samples. The trachyte and phonolite rocks show affinities with shoshonitic and ultrapotassic-potassic series.

Tuffaceous sandstone samples of the Lower Member and the sample from the matrix of the Upper Member have very high LOI (2.6–16.8 wt.%), so that we do not compare their contents of major elements with other block samples (Data Set S1). Tuffaceous sandstone samples are also rich in LILEs (e.g., Ba = 2,845–5,470 ppm, average = 4,055 ppm; Sr = 1,068–2,300 ppm, average = 2,300 ppm) and REEs (539–912 ppm, average = 692 ppm); however, they have lower values than the other block samples.

All the samples from the AVS have similar trace element and REE patterns that are very different from typical nonvolcanic sandstone lenses within the Xiyu Conglomerate (Figure 5).

4.4. $^{40}Ar/^{39}Ar$ Dating

We carried out $^{40}Ar/^{39}Ar$ dating on total of three samples from the Upper Member. Sample AT12-HS-CM is from a trachyte block. Both biotite and sanidine were analyzed for this sample to evaluate the reliability of $^{40}Ar/^{39}Ar$ dating on different minerals from the same sample. Fifteen crystals of biotite were analyzed of which one had a markedly older age (~140 Ma), which was interpreted as a xenocryst (Data Set S2 and Figure 6a). The other 14 crystals yielded a concordant age population with a weighted average age of 11.19 ± 0.03 Ma (2σ; Mean Square Weighted Deviation = 0.33, Probability = 0.99; Figure 6a). Fourteen

crystals of sanidine yielded a range of ages from ~11 to ~14 Ma (Data Set S3 and Figure 6a). Six crystals yielded a concordant age population with a weighted average age of 11.27 ± 0.03 Ma (2σ; MSWD = 1.2, P = 0.3). A single young crystal age of 11.16 ± 0.04 Ma is concordant with the biotite weighted mean age.

Sample AT12-HS-1 is a phonolite block from which we analyzed 13 sanidine crystals (Data Set S4 and Figure 6c). All crystals yield a homogenous age population with a weighted mean age of 11.07 ± 0.13 Ma (2σ; MSWD = 0.59, P = 0.85). The lower precision of this age compared with other results obtained in this study is because the analyses were done on a single collector MAP 215-50 mass spectrometer compared to a multi-collector ARGUS VI instrument, which gives the most precise results.

Fifteen sanidine crystals were dated for Sample AT12-04, which are from the matrix of the Upper Member (Data Set S5 and Figure 6d). $^{40}Ar/^{39}Ar$ dating showed that this sample contains two slightly older ages, with the rest of the 13 crystals yielding a homogenous age population with a weighted mean age of 11.24 ± 0.04 Ma (2σ; MSWD = 0.2, P = 1.0).

5. Interpretation

5.1. Eruption Age of the AVS

Samples from the Upper Member section yielded relatively consistent ages of ~11.2 Ma; however, weighted mean age from biotite and sanidine crystal populations from sample AT12-HS-CM bear a resolvable age difference of 0.08 ± 0.04 Ma (Figures 6a and 6b). It should be remembered that any single crystal within a population can reflect the age of the most recent eruption, but conversely could also yield the age of previous eruptions, and provide no information on the most recent eruption. This is particularly true if the youngest eruption is poor in sanidine or biotite. In other words, a population including several indistinguishable crystal ages could entirely consist of antecrysts or xenocrysts. In the case of Sample AT12-HS-CM, the age given by sanidine, indicates an age of 11.27 ± 0.03 Ma, whereas the youngest isolated sanidine crystal gave an age of 11.16 ± 0.04 Ma. Without the results obtained with the biotite crystals, the youngest 11.16 Ma sanidine age could be interpreted as an outlier affected by Ar loss, but, in fact, only the youngest sanidine crystal age is representative of the eruption age as it is fully consistent with the biotite population age of 11.19 ± 0.03 Ma. This suggests that the concordant population of sanidine crystals was inherited from a previous eruption. We conclude that the best age estimate of the eruption of the trachyte (AT12-HS-CM) is provided by the biotite (+single sanidine) population at 11.18 ± 0.03 (n = 14 bio + 1 san; MSWD = 0.41; P = 0.97) Ma.

The eruption age of the phonolite (AT12-HS-1) in the Upper Member is given by a homogenous crystal population of sanidine at 11.07 ± 0.13 Ma although the relatively low precision of this age prevents a relative comparison with the age of the trachyte. The sanidine extracted from the matrix sample (AT12-04) yielded a concordant age of 11.24 ± 0.04 Ma but is not clear to which eruption those crystals are associated with. The sanidine crystals in the matrix and trachyte and phonolite blocks suggest that the volcaniclastic deposits are younger than 11.07 ± 0.13 Ma.

Two ages of 11.49 ± 0.34 Ma and 10.94 ± 0.20 Ma obtained from biotite grains were published by Zheng et al. (2015a) for samples AT10-35 and AT10-34 from the Lower Member. Because the biotite crystals from these two samples were relatively small and were analyzed using a single collector machine, the dated ages had relatively larger errors. The age of 10.94 ± 0.20 Ma is only compatible with the one of the phonolite (11.07 ± 0.13 Ma) from the Upper Member and is younger than the ages of trachyte and matrix samples. This suggests that there was a delay between eruption and deposition of some components of the Upper Member. We interpret this delay to be the result of a slope failure of the source volcano (see section 5.3). Although the currently available data are unable to accurately determine the eruption period for the whole sequence, they imply that the eruptions likely lasted tens of thousands of years around ~11 Ma.

5.2. The Source of the Volcaniclastic Sequence

Previous studies suggest that ~11 Ma igneous rocks in the Pamir region are distributed around the KSES, including an alkaline volcanic-subvolcanic complex (Dunkeldik volcanic belt) (Figure 1d; e.g., Ducea et al., 2003; Hacker et al., 2005; Kooijman et al., 2017; Shaffer et al., 2017) and three alkaline plutons (Karibasheng, Kuzigan, and Zankan; Figure 1c; e.g., Dmitriev, 1976; Jiang et al., 2012; Ke et al., 2006; Lutkov

et al., 2005). Petrographic, petrological, geochronological, and whole-rock geochemical evidence indicates that the AVS in the foreland basin was most likely derived from the Dunkeldik volcanic belt.

1. The $^{40}Ar/^{39}Ar$ ages of the samples from the volcaniclastic sequence (ranging from 10.9 to 11.5 Ma) overlap those of the Dunkeldik complex rocks (10.8 ± 0.15 to 11.1 ± 0.15 Ma; Ducea et al., 2003; Kooijman et al., 2017; Shaffer et al., 2017).

2. Only the Dunkeldik volcanic belt shows unambiguous volcanic-subvolcanic lithofacies among ~11-Ma igneous rocks in the southeastern Pamir region (Dmitriev, 1976; Lutkov et al., 2005; Pan, 1996).

3. The volcaniclastic deposits and the Dunkeldik volcanic complex share similar rock types. Pseudoleucitite breccia, pseudoleucite phonolite blocks, and trachyte blocks of volcanic origin within the volcaniclastic sequence, respectively, correspond to the fergusite, pseudoleucitic tinguaite, and trachyte in the Dunkeldik volcanic complex (Ducea et al., 2003; Lutkov et al., 2005). The presence of minor crystalline calcite as veins along fractures in volcanic blocks within the volcaniclastic sequence shows that the volcanic rocks were intruded by carbonate fluid or melt, which is consistent with the carbonatite veins that cut the syenitoids of the Dunkeldik volcanic complex (Lutkov et al., 2005).

4. Samples from the AVS and the Dunkeldik volcanic complex show similar major element compositions and trace element and REE patterns (Figure 5). The trachyte and phonolite rocks show affinities with shoshonitic and ultrapotassic-potassic series, which is consistent with the rocks from the Dunkeldik volcanic complex. The average chemical compositions of syenite and tinguaite from the Dunkeldik volcanic complex plot in the middle of the range of phonolites from volcaniclastic members within the Xiyu Conglomerate (Figure 5a). The chemical composition of trachyte samples from the volcaniclastic sequence shows an evolutionary trend between syenite and quartz syenite from the Dunkeldik volcanic complex. Samples from the volcaniclastic sequence and Dunkeldik volcanic complex show very similar REE and trace element patterns, but these are both very different from those of typical sandstone lenses within the Xiyu Conglomerate (Figure 5c). The syenitoid of the Tashkorgan plutons shows average chemical compositions close to rocks of the Dunkeldik volcanic complex, which imply that there might be genetic relationships between these two complexes (Jiang et al., 2012). However, the granitoid of the Tashkorgan plutons exhibits distinctly higher SiO_2 and lower heavy REE than the volcaniclastic sequence.

5.3. Source to Sink Processes

Xenoliths from the Dunkeldik volcanic complex suggest that the Kohistan-Ladakh arc was subducted or foundered to depths of 90–100 km, reaching temperatures of ~1,000–1,100 °C beneath the Karakoram terrane (Ducea et al., 2003; Hacker et al., 2000; Shaffer et al., 2017). The eruption of the Dunkeldik magmas has been linked to a slab breakoff at a depth of >100 km under the Dunkeldik area (Jiang et al., 2012). The volcaniclastic sequence within the Xiyu Conglomerate was formed within this framework.

5.3.1. Upper Member

Our field investigations and petrologic observations suggest that it is dominated by volcaniclastic lithologies (Figure 3). The REE and trace element compositions of volcanic blocks and the matrix are very similar and much more concentrated than typical nonvolcanic sandstone lenses within the Xiyu Conglomerate (Figure 5). Nonerosive basal contacts, poor sorting, absence of stratification, and presence of abundant lapilli and blocks (Figures 2 and 3) all suggest that these sediments were formed by a fast-moving volcanic debris flow, that is, a lahar (Smith & Lowe, 1991). Jigsaw cracks are characteristic joint patterns within a debris-avalanche block. The joint planes of them are usually closed but may open wide and be separated by matrix due to crushing during transport, forming domains composed of clasts (e.g., Smith & Lowe, 1991; Ui et al., 2000; Yarnold & Lombard, 1989). The presence of jigsaw cracks within clasts (Figures S2a and S2b), domains of clasts (Figure 3e), and volcanic blocks (Figures 3a and S1) suggests that the volcanic debris flow was derived from a debris avalanche that initially formed by slope failure at a volcanic center(Scott et al., 2001; Smith & Lowe, 1991; Ui et al., 2000). The presence of jigsaw-fractured trachyte and schist clasts (Figures S1b and S1c), as well as trachyte and phonolite rocks with slight age differences (Figure 6), indicates that the slope failure likely incorporated different lava layers formed in different eruptive phases, as well as the Paleozoic metamorphic basement (Figure 7). Lenses and belts of lava with plastic-flow-like shapes and/or red oxidation edges are particularly noteworthy (Figures 3f and S1). Their presence suggests that these lavas were still hot when they mixed with other clasts (Smith & Lowe, 1991). We infer that the volcanic slope was
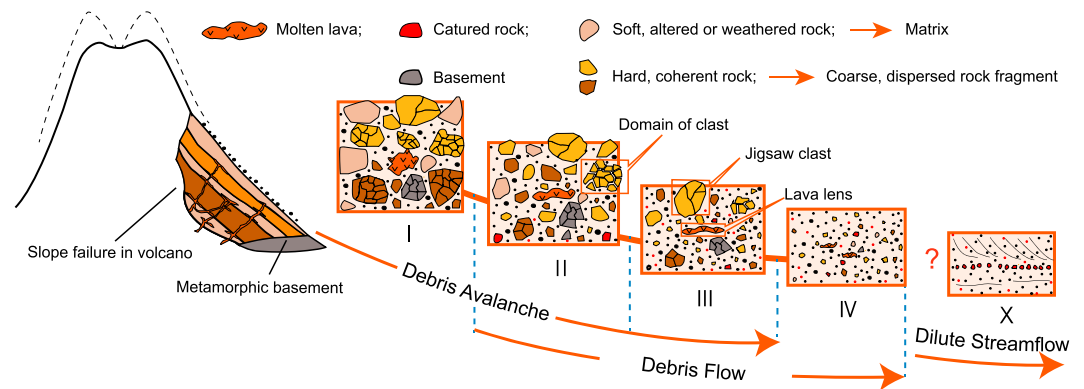
Figure 7. Diagram showing the interpreted source to sink process of the volcaniclastic sequence. Based on Scott et al. (2001). See text for detailed interpretation.

destabilized by magmatic intrusion or associated hydrovolcanism, as indicated by the presence of pseudoleucite and carbonate veins within the volcanic blocks prior to slope failure triggered by eruptive activity in the Dunkeldik area. The slope failure transformed into a debris avalanche and subsequently to a debris flow as detritus traveled rapidly downslope with more and more coarse clasts gradually being deposited and/or disaggregate into smaller fragments.

Figure 7 shows the emplacement from a landslide to a cohesive debris flow and further to a streamflow. As the landslide triggered by an eruption occurred, a rapid inertial, granular debris avalanche formed (Stage I). The clasts of the debris avalanche in Stage I would have been dominated by brecciated jigsaw-fractured megaclasts generated by dilation during failure (Smith & Lowe, 1991). Subsequently, the proportion of mega-clasts decreased as these clasts disaggregated and/or were deposited, especially the poorly consolidated or weaker ones. This process formed more and more fine-grained material during downslope transport (Stages II and III). Stages II and III are the middle stages in the transformation from a debris avalanche to a cohesive debris flow. Deposits formed in Stages II and III may be regarded as either debris avalanche or debris flow (Scott et al., 2001; Smith & Lowe, 1991). Debris flows exhibit strength or resistance to shear that derive from grain collisions and cohesion between clay- to silt-sized ash particles, so that they are able to carry megaclasts and flow with laminar motion for >100 km without further transformation (e.g., Fisher & Schmincke, 1984; Scott et al., 2001; Smith, 1986; Smith & Lowe, 1991). The presence of lenses or belts of lava with plastic-flow-like shapes, which are indicative of a lack of disturbance, provides robust evidence for the laminar motion of the debris flow. Further, downstream changes may result in debris flow dominated by sediments without any megaclasts (Stage IV), hyperconcentrated flow, or dilute streamflow (Stage V), as a result of depositional and dilution processes (Scott et al., 2001; Smith & Lowe, 1991). We suggest that the Upper Member was formed during Stage III, on the topographic slope, when the velocity of the debris flow decreased below the threshold to maintain laminar flow, resulting the entire flow stopping en masse rather abruptly and forming a massive, matrix-supported mixture dominated by volcaniclastic materials with mega-clasts and lenses and belts of lava dispersed (Figure 7).

5.3.2. Lower Member

Both petrologic observations and geochemical data demonstrate that the tuffaceous sandstone is dominated by volcaniclastic clasts, mixed with minor nonvolcanic grains (Figures 4 and 5). The development of cross bedding and parallel bedding in the Lower Member indicates that transport was in the form of dilute stream-flow (Stage V in Figure 7), in which particles are carried in the water by turbulence and traction processes (e.g., Fisher & Schmincke, 1984; Smith, 1986; Smith & Lowe, 1991). Further interpretation of the initial transport mechanisms of the flows is difficult. The dilute streamflow may be transformed from initial debris flow or hyperconcentrated flow as the result of dilution by water (Figure 7). Alternatively, they may have formed directly by mixture of loose volcaniclastic clasts or pyroclastic flows/surges with water (Smith & Lowe, 1991). The fact that the tuffaceous sandstones are predominantly composed of clasts of volcanic origin indicates that the dilute streamflows were formed when the source region was able to provide abundant clasts, which usually occurred during or soon after eruption, as observed at many modern volcanoes (e.g., Johnson

& Palma, 2015; Pierson, 1995; Umbal & Rodolfo, 1996; Vallance, 1999). The intercalated layers of conglomerate resembling typical Xiyu Conglomerate are interpreted to be deposited between eruptions. We proposed that the Lower Member does not represent a single depositional event, but rather a sequence formed by remobilization of material emitted in several eruptions spanning tens of thousands of years, consistent with the $^{40}Ar/^{39}Ar$ dating results.

Although this study focuses on the AVS, we further discuss the relationship between the AVS and the "ash" layers (termed tuffaceous sandstone in the terminology of this study) at the Kekeya section (Figure 1c; Sun et al., 2015; Zheng et al., 2015a, 2015b). The ash layers have the same ages and similar compositions as the Lower Member tuffaceous sandstone from the AVS but do not contain gravels or debris flow deposits. Several lines of evidence indicate that they are (reworked) air fall ash deposits, rather than distal fluvial sediments of the AVS. (1) The ash layers at Kekeya are intercalated within eolian silt, which implies relatively high paleotopography in the depositional environment that lacks of permanent stream action (Zheng et al., 2006). This is very different from the upper part of the Aertashi section, which is dominated by massive conglomerates with minor sandstones. (2) The clasts of Xiyu Conglomerate in the Kekeya section and the Aertashi section show totally different compositions, with the former dominated by angular to subangular sedimentary rocks and the latter dominated by rounded to subrounded igneous and matamorphic rocks. (3) Paleocurrent analyses of the Xiyu Formation yielded east to NW flow directions at Aertashi (Zheng et al., 2010, and this study) and northward flow direction at Kekeya (Zheng et al., 2006). (4) Isopach maps of different units of the Neogene strata in the southwestern Tarim Basin indicate a depression to the NNE of Kekeya (Wei et al., 2013), inconsistent with the idea of sediments being supplied via Aertashi. We suggest that the ash layers were formed by air fall processes at Kekeya or upstream of this location, which is consistent with the finding of minor syneruptive zircon in sandstone lenses within the Xiyu Conglomerates at Sanju further east (Cao et al., 2015).

6. Discussion

6.1. Constraints for Evolution of the Tashkorgan-Yarkand River

The Tashkorgan-Yarkand River was variously proposed to form during pre-Miocene (Sobel et al., 2011), middle Miocene to post-Pliocene (Cao et al., 2014), or recently (Blayney et al., 2016; Clift et al., 2017). The radio-isotopic ages of the AVS, in combination with magnetostratigraphy, provides a high-resolution geochronological framework for the Cenozoic continental deposits in the Pamir-Western Kunlun foreland basin (Figure 2; Zheng et al., 2015a). Therefore, we are able to reconstruct an evolutionary history for the Tashkorgan-Yarkand River by linking the source and sink of the AVS and scrutinizing the published provenance data.

Figure 8 shows the previously published detrital zircon U-Pb age spectra of both modern river sand of potential source regions of the Tashkorgan-Yarkand River and the sedimentary rocks that might record the river evolution (Blayney et al., 2016; Carrapa et al., 2014; Clift et al., 2017; Lukens et al., 2012; Rittner et al., 2016). In Figure 8, we only present the ≤1,000 Ma ages as they are critical components for provenance identification in this region (e.g., Blayney et al., 2016; Clift et al., 2017). The modern samples from the Northern Pamir (Karakul-Mazar terrane; Figure 8a), Central Pamir (Figure 8b), and Southern Pamir-Karakoram (Figure 8c) show single predominant age peaks of Triassic, Cretaceous, and Paleogene, respectively. The modern river sand derived from the Western Kunlun (Figure 8d), however, has two main age peaks of Permian-Triassic (200–300 Ma) and Ordovician-Devonian (400–500 Ma). The data of the main stream of the Tashkorgan-Yarkand River exhibit a major peak of Cretaceous, and two subordinate peaks of Ordovician-Devonian (400–500 Ma) and Triassic (Figure 8f), which is consistent with the catchment of this river covering the Southern Pamir-Karakoram and the Western Kunlun (Figure 1c). The ≥15-Ma sedimentary samples of the Aertashi section were collected from terrestrial red beds underlying the Xiyu Formation (Blayney et al., 2016). Because they have similar age spectra showing double peaks of Permian-Triassic (200–300 Ma) and Ordovician-Devonian (400–500 Ma; Blayney et al., 2016), the zircon ages of these samples were plotted together in Figure 8j. These samples show similar spectra to those of the modern sand samples derived from the Western Kunlun and no significant amount of zircon grains from the Karakul-Mazar terrane and the Central Pamir. This indicates a source of the Western Kunlun for these samples or limited exhumation in other terranes. The latter seems unlikely as the domes within these regions experienced strong exhumation in the early Miocene (e.g., Rutte,
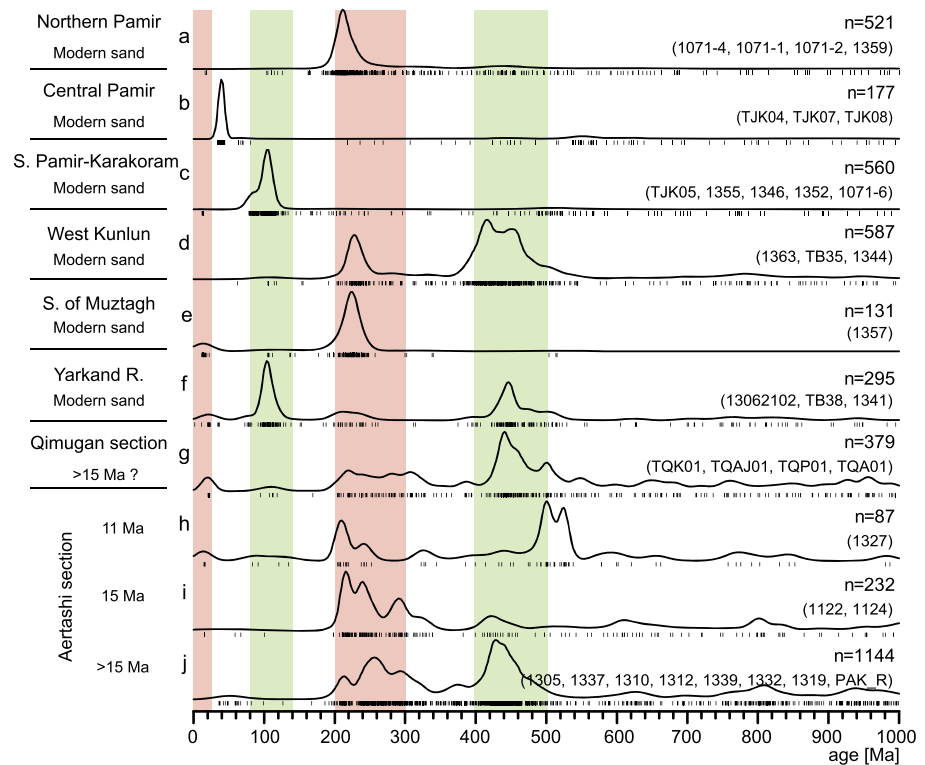
Figure 8. Kernel density estimate plots of zircon U-Pb ages spanning 1,000 m.y. from both modern sand and older sandstone samples considered in this study. Data of modern sand are from compilation of Blayney et al. (2016), Carrapa et al. (2014), Clift et al. (2017), Lukens et al. (2012), and Rittner et al. (2016). Data of older sedimentary rocks from the Aertashi section and the Qimugan section are from Blayney et al. (2016) and Cao et al. (2014), respectively. Sample names are indicated within brackets. An question (?) mark after an age denotes the age is uncertain.

Ratschbacher, Khan, et al., 2017; Stearns et al., 2013; Stübner et al., 2013). Sparse Paleogene zircon grains in these samples were also inferred to come from the Qiangtang terrane by a northward flowing river system from the Western Kunlun (Blayney et al., 2016). If there was an embryonic paleo-Tashkorgan-Yarkand river at >15 Ma, the catchment basin of this river would appear to be largely within the piedmont of the Eastern Pamir (Figure 9b). The ~15 Ma sample is from the massive, gray sandstone at the base of the Xiyu Formation (Figure 2; Blayney et al., 2016). The zircon ages of this sample differ from the underlying older samples in showing a significant increase in the Triassic grains and a decrease in the Ordovician-Devonian (400–500 Ma) grains (Figure 8i). This has been interpreted as an increased sediment influx from the Northern Pamir (Karakul-Mazar terrane) as it was northward indented in the vicinity of the Aertashi (Blayney et al., 2016). However, the Triassic grains could also be derived from the south side of the Muztaghata dome, which is part of the Karakul-Mazar terrane as well (Figures 1b and 1c). The abundance of Triassic detrital zircon in the northern tributary of the Tashkorgan River (Figure 8e), which originates from the southern Muztaghata dome (Figure 9a), supports our inference. We suggest that it was the paleo-Tashkorgan River that connected the Tashkorgan and the Aertashi at ~15 Ma (Figure 9c), considering that this river had reached the Dunkeldik region and provided a channel for the transportation of the AVS at ~11 Ma (Figure 9d) as we will discuss next.

The ~11 Ma emplacement of the AVS provides important constraints for the evolution of the Tashkorgan-Yarkand River. The presence of Aertashi volcanic debris is indicative of direct flow from Dunkeldik to Aertashi at ~11 Ma, although there is no channel linking the above two locations at present (Figure 9a). The Muztaghata dome has been suggested to be the eastward continuation of the Muskol-Shatput dome of the Central Pamir (Figure 9a) and was formed by N-S extension along E-W trending normal-sense shear zones in the early Miocene (Rutte, Ratschbacher, Khan, et al., 2017) or middle Miocene (Robinson et al., 2007). Today, the above normal-sense shear zones still show an approximately E-W trending geometry (Figure 9a), indicating that there should have been no significant relative N-S displacement between
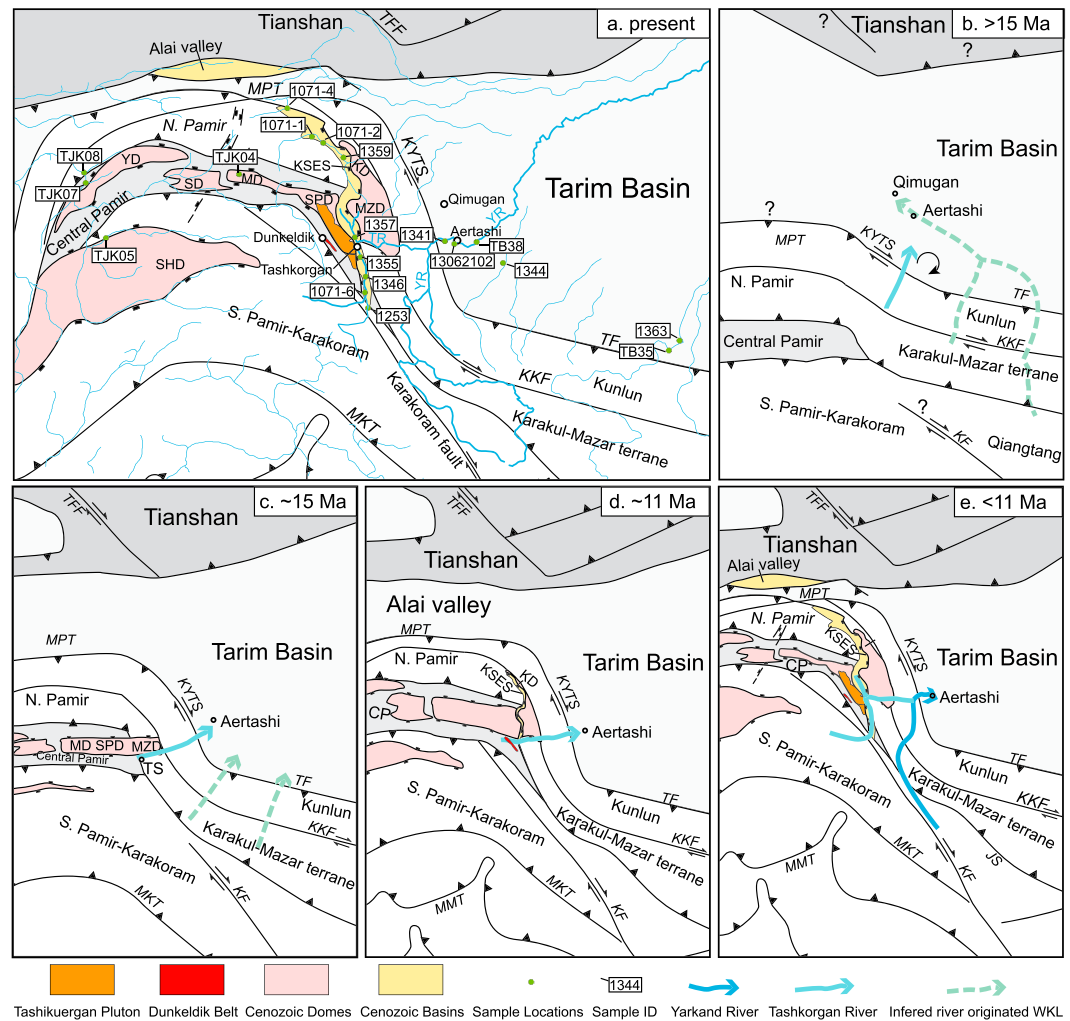
Figure 9. Distribution of reviewed samples and proposed Cenozoic tectonic and paleogeographic evolution of the Pamir salien. (a) Simplified structure map of present and distribution of reviewed samples. (b) Proposed paleogeographic pattern prior to ~15 Ma. (c) Proposed paleogeographic pattern at ~15 Ma. (d) Proposed paleogeographic pattern at ~11 Ma. The KSES started to west-east dip slip. (e) Proposed paleogeographic pattern after ~11 Ma. Stuctures are based on Bakirov et al. (2001), Burtman and Molnar (1993), Cao, Bernet, et al. (2013), Cao, Wang, et al. (2013), Cowgill (2010), Robinson et al. (2004, 2007), Rutte, Ratschbacher, Khan, et al. (2017), Rutte, Ratschbacher, Schneider, et al. (2017), Sobel et al. (2013), and Stübner et al. (2013). Rivers are based on Blayney et al. (2016) and this study. CP: Central Pamir, DK: Dunkeldik, KF: Karakoram Fault, KKF: Karakash Fault, MKT: Main Karakoram Thrust, MMT: Main Mantle Fault, TF: Tiklik Fault, TFF: Talas-Fergana Fault, TS: Tashkorgan. Other abbreviations are the same with Figure 1. Question (?) marks in (b) denote the positions of the faults are uncertain.

Dunkeldik (Central Pamir) and the Tashkorgan valley (Eastern Pamir) since initial activity of these shear zones in the early Miocene (Rutte, Ratschbacher, Khan, et al., 2017). As a result, we suggest that the Aertashi volcanic debris flow was most likely transported through the paleo-Tashkorgan River rather than other rivers and that this river must have reached to the Central Pamir by ~11 Ma (Figure 9d). The ~11 Ma sample in Figure 8h was from the Lower Member tuffaceous sandstone (Figure 2). Detrital zircon ages of this sample show a similar Triassic peak as the ~15 Ma samples (Figures 8h and 8i) but differ from other samples in showing an unusual predominant Cambrian peak. The predominant Cambrian peak could represent the focused exhumation of the surrounding rocks of the Dunkeldik volcanic rocks due to eruptions, which is consistent with the dominance of Cambrian metatuffite, orthogneiss, and leucosome within the Central Pamir domes (Figure 3 in Rutte, Ratschbacher, Schneider, et al., 2017). Although only sparse mid-Miocene zircon grains were detected in the ~11 Ma tuffaceous sandstone, it is not surprising considering that the volcanic rocks in Dunkeldik are likely poor in zircon fertility as indicated by our mineral separation work. Interestingly, no

Eocene zircon ages, which dominate the modern surficial sand samples in the Central Pamir, are detected in the ≤15 Ma samples from the Aertashi section (Figures 8h and 8i). We interpret this as insufficient exhumation of the Eocene plutons within the Central Pamir prior to 11 Ma. The Central Pamir might be dominated by metamorphic rocks at that time, which is consistent with the abundant occurrence of the Cambrian zircon grains within the ~11 Ma tuffaceous sandstone sample from the AVS (Figure 8h).

Although the timing of initiation of extension at the southern end of the KSES is still unclear, the exhumation of the footwall of the east dipping Tashkorgan normal fault (Figure 1c) would lead to the formation of a N-S trending channel in the Tashkorgan valley. Subsequently, the connection between the Central Pamir and the Tashkorgan valley would gradually be cut off. Because the initial extension of the KSES was variously dated at ~12–10 Ma (Rutte, Ratschbacher, Khan, et al., 2017), 8–7 Ma (Robinson et al., 2007), or 6–5 Ma (Cao, Bernet, et al., 2013), we suggest that the N-S trending upper reach of the paleo-Tashkorgan River started to develop after ~11 Ma following the onset of extension of the KSES (Figure 9e).

According to the existing provenance data, the Yarkand River was established after ~11 Ma (Figure 9e). The Southern Pamir-Karakoram, where the headwaters of the modern Yarkand River are derived from, is composed of a large amount of Cretaceous igneous rocks (Figure 1c and 8f). However, only sparse Cretaceous zircon grains were detected in the ≥11 Ma samples from the Aertashi section (Figures 8h–8j). In the Qimugan section, Cao et al. (2014) detected a minor Cretaceous age peak of detrital zircon in sedimentary rock samples (Figure 9g), the sedimentary ages of which were proposed to span from the early Miocene to the Pliocene (Cao et al., 2014). The presence of ~20 Ma peak and the absence of ~11 Ma peak in these samples made Cao et al. (2014) conclude that the Cretaceous and ~20 Ma zircon grains should have been derived from the Southern Pamir-Karakoram instead of the Tashkorgan region, otherwise the ~11 Ma zircon should have been found in these samples if this river reached the Tashkorgan (Figure 1c). Cao et al. (2014) further proposed that the paleo-Yarkand River similar to the modern pattern formed in the early Miocene and that the paleo-Tashkorgan River did not reach to the Tashkorgan region by the Pliocene. However, lines of evidence do not support their interpretations: (1) the samples from the Qimugan section were collected from the sequence underlying the Xiyu Conglomerate (Cao et al., 2014). According to our age constraints, these samples are likely older than ~15 Ma (Figure 2). This would explain why the ~11 Ma zircon from the Tashkorgan plutons have not been recorded in these samples. Alternatively, insufficient exhumation of the Tashkorgan plutons or limited catchment of the upper stream might also account for the absence of the ~11 Ma zircon. (2) Cai et al. (2017) reported substantial ~20 Ma granites around the Muztaghata dome, which may have provided the ~20 Ma zircon in the Qimugan section rather than the Karakoram batholith. (3) The minor Cretaceous zircon within the Qimugan section could also derived from the Muztaghata dome as Robinson et al. (2007) detected Cretaceous oscillatory zoned zircon from mylonitic granite in this dome. (4) The Qimugan samples show two predominant peaks of 200–300 Ma and 400–500 Ma, which is similar with the >15 Ma Aertashi samples (Figures 8d and 8g) rather than the modern Yarkand samples (Figure 8f). Considering that none of the presently published ≥11 Ma samples contain significant amounts of Cretaceous grains, which dominate in the modern catchment of the Yarkand River (Figure 8f), we suggest that this river was established after ~11 Ma (Figure 9e).

In summary, our results suggest that the Tashkorgan-Yarkand River system has experienced a multistage evolutionary history. The Aertashi and Qimugan area likely received Western Kunlun-dominated sediment input before ~15 Ma (Figure 9b). Meanwhile, the paleo-Tashkorgan River that was largely confined within the piedmont of the Pamir marginal range may have formed at the same time (Figure 9a). The paleo-Tashkorgan River cuts back into the internal regions of the Eastern Pamir, the Tashkorgan region at ~15 Ma (Figure 9c), and, subsequently, the Central Pamir before ~11 Ma (Figure 9d). The N-S trending main upstream channel of this river started to develop after ~11 Ma (Figure 9e). The Yarkand River originating from the Southern Pamir-Karakoram was established after ~11 Ma as well (Figure 9e).

6.2. Constraints on Motion Between Pamir and Tarim

The spatiotemporal evolution of the Pamir salient is another highly controversial issue, especially whether it was formed in the pre-Cenozoic, early Cenozoic, or late Miocene (e.g., Burtman & Molnar, 1993; Chapman et al., 2017; Chen et al., 2018; Coutand et al., 2002; Cowgill, 2010; Kufner et al., 2016; Rutte, Ratschbacher, Khan, et al., 2017). The presence and the nature of the volcanic debris flow at the Aertashi provide an important constraint on the tectonic landform of the Pamir-Tarim system during the middle Miocene.

The emplacement of the Aertashi volcanic debris flow indicates limited strike-slip motion between the Pamir and the Tarim since ~11 Ma. Today, using the dextral KYTS as a demarcation, the upper and lower reaches of the Tashkorgan River flow eastward rather linearly despite crossing several north striking structures. This indicates a lack of recently significant N-S strike slip of these structures (Sobel et al., 2011). We propose that the upper reach of this river has flown eastward since the early Miocene considering that the whole of the Eastern Pamir has no significant rotation since then (Bosboom, Dupont-Nivet, Huang, et al., 2014). Paleocurrent measurements in this study indicate a west-east trending lower reach of the paleo-Tashkorgan-Yarkand River around Aertashi at ~11 Ma (Figure 2). The link between the upper reach and the lower reach of this river at ~11 Ma results into two interpretations of the geometry of channel: (1) the channel ran across the KYTS with no significant north-south offset at that time and (2) the Paleo-Tashkorgan-Yarkand River has a west-east trending upper reach and lower reach with the middle part flowing northward along the KYTS (S-shaped channel of the whole river). We prefer the first interpretation as the KYTS is a dextral stike-slip fault system, the lower reach should be left to the south of the upper reach (resulting in a Z-shaped channel for the whole river) rather than to the north (resulting in a S-shaped channel of the whole river) if the KYTS had a fast slip rate at ~11 Ma. In this case, the paleo-Tashkorgan River had an overall E-W trending geometry with limited N-S offset between the upper and the lower reaches at ~11 Ma. Therefore, the transport of volcanic debris flow through the eastward paleo-Tashkorgan River to the Aertashi indicates that there has been no significant strike-slip offset between the Dunkeldik (Central Pamir) and the Aertashi (Tarim) since ~11 Ma.

Moreover, the run-out length limit of volcanic debris flows does not support the envision that the Pamir has northward moved relative to the Tarim by a large distance since ~11 Ma. Statistical data of observed volcanic debris flows indicate <120 km of run-out lengths for most of them (Carrasco-Núñez et al., 1993; Iverson, 1997; Scott et al., 2001; Siebert et al., 1987; Tost et al., 2014; Vallance & Scott, 1997), except one report, which inferred a length of ~170 km for a volcanic debris flow in southwestern Colombia (Scott et al., 2001). The present linear distance between the Dunkeldik Volcanic Belt and the Aertashi is ~160 km. This distance should be smaller prior to the extension of the KESE at ~11 Ma (Rutte, Ratschbacher, Khan, et al., 2017). Nevertheless, it should be larger than 157 km as the Tashkorgan fault has <3 km east-west extension (Robinson et al., 2007). On the other hand, the sinuosity of the channel would yield a longer channel length than the actual linear distance. Therefore, the 157 km is a conservative estimate for the actual run-out length of the Aertashi volcanic debris flow. Such a run-out length is close to the upper limit of observed run-out length data of volcanic debris flows. In any case, the empirical data (e.g., Tost et al., 2014) do not support the model that the Pamir was still located south of its present position at a large distance at ~11 Ma (e.g., Kufner et al., 2016; Rutte, Ratschbacher, Khan, et al., 2017), otherwise the volcanic debris flow was unlikely able to flow to the Aertashi.

The above arguments are also compatible with thermochronologic and structural evidence (e.g., Cao, Wang, et al., 2013; Rutte, Ratschbacher, Khan, et al., 2017; Sobel et al., 2011). The initial east-west extension of the KSES has been assigned to ~8–7 Ma (Robinson et al., 2004; Thiede et al., 2013) or ~6–5 Ma (Cao, Bernet, et al., 2013), based on AFT, ZFT, and $^{40}Ar/^{39}Ar$ ages from the footwall of the Kongur Shan Fault. However, these low-intermediate-T thermochronometers may only document the minimum age of the KSES if erosion has removed evidence of earlier cooling. Recently, Rutte, Ratschbacher, Khan, et al. (2017) reinterpreted the published thermochronologic evidence along the KSES and proposed that the timing of onset of extension along the KSES may have been ~12–10 Ma triggered by the westward collapse of the Pamir into the Tajik depression to the west (Figure 9d). To the east, Cao, Wang, et al. (2013) dated the recent thrusting of the northern KYTS along the Kizilto transect using ~10–6 Ma AFT cooling ages. AHe ages of ~10–9 Ma from Sobel et al. (2011) in the Yarkand transect crossing the KYTS may also recorded this cooling event. The synchronous approximately E-W extension of the KSES within the Pamir and the approximately E-W compression along the KYTS between the Pamir and the Tarim at ~12–9 Ma implies that Pamir deformation was dominated by E-W collapse rather than N-S fast strike-slip motion. The strike-slip motion of the Pamir relative to the Tarim, which was accommodated by the dextral KYTS, probably has largely decreased by this time. According to the model of Sobel et al. (2011), the deceleration of the KYTS may primarily reflect that the velocity of Tarim increased to the same level of the Pamir and that the Pamir and the Tarim may have moved northward together from this time (Figure 9e).

In summary, both the emplacement of the Aertashi volcanic debris flow and the regional geological evidence indicate that there has been no significant northward indention of the Pamir relative to the Tarim since ~11 Ma. This argument supports a pre-Cenozoic formation (e.g., Chapman et al., 2017; Chen et al., 2018;

Coutand et al., 2002) or Eocene to early Miocene indention of the Pamir salient (e.g., Bosboom, Dupont-Nivet, Huang, et al., 2014; Burtman & Molnar, 1993; Cao, Wang, et al., 2013; Sobel & Dumitru, 1997). We suggest that hundreds of kilometers of displacement between the Pamir and the Tarim during the late Miocene (e.g., Kufner et al., 2016; Rutte, Ratschbacher, Khan, et al., 2017) are unlikely.

7. Conclusions

We identified the Aertashi Volcaniclastic Sequence within the Xiyu Conglomerate in the Pamir-West Kunlun foreland basin and divided the sequence into a Lower and Upper Member. Radioisotopic dating on sanidine and biotite grains from different layers and different petrofacies within the volcaniclastic unit shows consistent ages of ~11 Ma. Petrographic, geochronological, and whole-rock geochemical evidence indicates that the volcaniclastic sequence was likely derived from the Dunkeldik volcanic complex. The sediments of the Lower Member were transported in the form of dilute streamflows before deposition. The dilute streamflows most likely formed during or soon after the eruptions, when the source region provided abundant clasts. The Upper Member was formed by a fast-moving volcanic debris flow, likely transformed from an initial slope failure at the volcanic center, which is inferred to have been triggered by a volcanic eruption.

Based on the provenance/transport analysis of the volcaniclastic sequence, as well as published provenance data review, we reconstruct the Cenozoic evolution of the Tashkorgan-Yarkand River system. We suggest that the Tashkorgan-Yarkand River has experienced a multistage evolutionary history. The paleo-Tashkorgan River that was largely confined within the piedmont of the Pamir marginal range may have formed prior to ~15 Ma. This river cuts back into the internal regions of the Eastern Pamir, the Tashkorgan region at ~15 Ma, and after which it has eroded the Central Pamir by ~11 Ma. The N-S trending upper reach of this river started to develop after ~11 Ma following the onset of extension of the KSES, while the source to sink linkage between the Central Pamir and the Tarim was gradually cut off accompanying the exhumation of the footwall of the Tashkorgan fault. The Yarkand River originating from the Southern Pamir-Karakoram was established after ~11 Ma because no significant sediment input from these areas was recorded at this time. The ~11 Ma emplacement of the volcaniclastic sequence, together with the deformation evidence of the Pamir, does not support a large-scale strike-slip motion along the KYTS between Pamir and the Tarim after ~11 Ma. This supports an earlier northward indention or pre-Cenozoic formation of the arcuate Pamir salient, while hundreds of kilometers of slip displacement between the Pamir and the Tarim during the late Miocene are unlikely.

References

Bakirov, A., Ghes, M., Maksumova, R., & Gusak, L. (2001). Geodynamic map of Kyrgyzstan.1:500,000. Bishkek: Institute of geology, National Academy of Science.

Bande, A., Sobel, E. R., Mikolaichuk, A., & Acosta, V. T. (2015). Talas–Fergana Fault Cenozoic timing of deformation and its relation to Pamir indentation. *Geological Society, London, Special Publications*, *427*, SP427.1. https://doi.org/10.1144/SP427.1

Bazhenov, M. L. (1993). Cretaceous paleomagnetism of the Fergana Basin and adjacent ranges, central Asia: Tectonic implications. *Tectonophysics*, *221*(2), 251–267. https://doi.org/10.1016/0040-1951(93)90335-H

Blayney, T., Najman, Y., Dupont-Nivet, G., Carter, A., Millar, I., Garzanti, E., et al. (2016). Indentation of the Pamirs with respect to the northern margin of Tibet: Constraints from the Tarim basin sedimentary record. *Tectonics*, *35*, 2345–2369. https://doi.org/10.1002/2016TC004222

Bosboom, R., Dupont-Nivet, G., Grothe, A., Brinkhuis, H., Villa, G., Mandic, O., et al. (2014a). Linking Tarim Basin sea retreat (west China) and Asian aridification in the late Eocene. *Basin Research*, *26*(5), 621–640. https://doi.org/10.1111/bre.12054

Bosboom, R., Dupont-Nivet, G., Grothe, A., Brinkhuis, H., Villa, G., Mandic, O., et al. (2014b). Timing, cause and impact of the late Eocene stepwise sea retreat from the Tarim Basin (west China). *Palaeogeography Palaeoclimatology Palaeoecology*, *403*, 101–118. https://doi.org/10.1016/j.palaeo.2014.03.035

Bosboom, R., Dupont-Nivet, G., Huang, W., Yang, W., & Guo, Z. (2014). Oligocene clockwise rotations along the eastern Pamir: Tectonic and paleogeographic implications. *Tectonics*, *33*, 53–66. https://doi.org/10.1002/2013TC003388

Bosboom, R. E., Dupont-Nivet, G., Houben, A. J. P., Brinkhuis, H., Villa, G., Mandic, O., et al. (2011). Late Eocene Sea retreat from the Tarim Basin (west China) and concomitant Asian paleoenvironmental change. *Palaeogeography Palaeoclimatology Palaeoecology*, *299*(3–4), 385–398. https://doi.org/10.1016/j.palaeo.2010.11.019

Boynton, W. V. (1984). Chapter 3—Cosmochemistry of the rare earth elements: Meteorite studies. In P. Henderson (Ed.), *Developments in geochemistry* (Vol. 2, pp. 63–114). Amsterdam: Elsevier. https://doi.org/10.1016/B978-0-444-42148-7.50008-3

Burtman, V. S. (2000). Cenozoic crustal shortening between the Pamir and Tien Shan and a reconstruction of the Pamir-Tien Shan transition zone for the Cretaceous and Palaeogene. *Tectonophysics*, *319*(2), 69–92. https://doi.org/10.1016/S0040-1951(00)00022-6

Burtman, V. S., & Molnar, P. (1993). Geological and geophysical evidence for deep subduction of continental crust beneath the Pamir. *Geological Society of America Special Papers*, *281*, 1–76. https://doi.org/10.1130/SPE281-p1

Cai, Z., Xu, Z., Cao, H., Robinson, A. C., Li, G., & Xu, X. (2017). Miocene exhumation of northeast Pamir: Deformation and geo/thermochronological evidence from western Muztaghata shear zone and Kuke ductile shear zone. *Journal of Structural Geology*, *102*, 130–146. https://doi.org/10.1016/j.jsg.2017.07.010

Cao, K., Bernet, M., Wang, G. C., van der Beek, P., Wang, A., Zhang, K. X., & Enkelmann, E. (2013). Focused Pliocene-Quaternary exhumation of the eastern Pamir domes, western China. *Earth and Planetary Science Letters*, *363*, 16–26. https://doi.org/10.1016/j.epsl.2012.12.023

Cao, K., Wang, G.-C., Bernet, M., van der Beek, P., & Zhang, K.-X. (2015). Exhumation history of the West Kunlun Mountains, northwestern Tibet: Evidence for a long-lived, rejuvenated orogen. *Earth and Planetary Science Letters*, *432*, 391–403. https://doi.org/10.1016/j.epsl.2015.10.033

Cao, K., Wang, G.-C., van der Beek, P., Bernet, M., & Zhang, K.-X. (2013). Cenozoic thermo-tectonic evolution of the northeastern Pamir revealed by zircon and apatite fission-track thermochronology. *Tectonophysics*, *589*, 17–32. https://doi.org/10.1016/j.tecto.2012.12.038

Cao, K., Xu, Y., Wang, G., Zhang, K., van der Beek, P., Wang, C., et al. (2014). Neogene source-to-sink relations between the Pamir and Tarim Basin: Insights from stratigraphy, detrital zircon geochronology, and whole-rock geochemistry. *Journal of Geology*, *122*(4), 433–454. https://doi.org/10.1086/676478

Carrapa, B., Mustapha, F. S., Cosca, M., Gehrels, G., Schoenbohm, L. M., Sobel, E. R., et al. (2014). Multisystem dating of modern river detritus from Tajikistan and China: Implications for crustal evolution and exhumation of the Pamir. *Lithosphere*, *6*(6), 443–455. https://doi.org/10.1130/L360.1

Carrasco-Núñez, G., Vallance, J. W., & Rose, W. I. (1993). A voluminous avalanche-induced lahar from Citlaltépetl volcano, Mexico: Implications for hazard assessment. *Journal of Volcanology and Geothermal Research*, *59*(1-2), 35–46. https://doi.org/10.1016/0377-0273(93)90076-4

Chapman, J. B., Carrapa, B., Ballato, P., DeCelles, P. G., Worthington, J., Oimahmadov, I., et al. (2017). Intracontinental subduction beneath the Pamir Mountains: Constraints from thermokinematic modeling of shortening in the Tajik fold-and-thrust belt. *GSA Bulletin*, *129*(11–12), 1,450–1,471. https://doi.org/10.1130/B31730.1

Chen, X., Chen, H., Lin, X., Cheng, X., Yang, R., Ding, W., et al. (2018). Arcuate Pamir in the Paleogene? Insights from a review of stratigraphy and sedimentology of the basin fills in the foreland of NE Chinese Pamir, western Tarim Basin. *Earth-Science Reviews*, *180*, 1–16. https://doi.org/10.1016/j.earscirev.2018.03.003

Chengdu Institute of Geology and Mineral Resources, C. A. of G. S. (1989). Geological map of Qinghai-Xizang (Tibet) plateau and adjacent areas (1: 1,500,000). Beijing Geological Pub House.

Clark, M. K., Schoenbohm, L. M., Royden, L. H., Whipple, K. X., Burchfiel, B. C., Zhang, X., et al. (2004). Surface uplift, tectonics, and erosion of eastern Tibet from large-scale drainage patterns. *Tectonics*, *23*, TC1006. https://doi.org/10.1029/2002TC001402

Clift, P. D., Zheng, H., Carter, A., Böning, P., Jonell, T. N., Schorr, H., et al. (2017). Controls on erosion in the western Tarim Basin: Implications for the uplift of northwest Tibet and the Pamir. *Geosphere*, *13*(5), 1747–1765. https://doi.org/10.1130/GES01378.1

Coutand, I., Strecker, M. R., Arrowsmith, J. R., Hilley, G., Thiede, R. C., Korjenkov, A., & Omuraliev, M. (2002). Late Cenozoic tectonic development of the intramontane Alai Valley, (Pamir-Tien Shan region, central Asia): An example of intracontinental deformation due to the Indo-Eurasia collision. *Tectonics*, *21*(6), 1053. https://doi.org/10.1029/2002TC001358

Cowgill, E. (2010). Cenozoic right-slip faulting along the eastern margin of the Pamir salient, northwestern China. *Geological Society of America Bulletin*, *122*(1–2), 145–161. https://doi.org/10.1130/B26520.1

Dmitriev, E. A. (1976). *Cenozoic potassium alkaline rocks of the Eastern Pamirs*. Dushanbe: Donish.

Ducea, M. N., Lutkov, V., Minaev, V. T., Hacker, B., Ratschbacher, L., Luffi, P., et al. (2003). Building the Pamirs: The view from the underside. *Geology*, *31*(10), 849–852. https://doi.org/10.1130/G19707.1

Fisher, R. V. (1961). Proposed classification of volcaniclastic sediments and rocks. *Geological Society of America Bulletin*, *72*(9), 1409–1414. https://doi.org/10.1130/0016-7606(1961)72[1409:PCOVSA]2.0.CO;2

Fisher, R. V., & Schmincke, H.-U. (1984). *Pyroclastic rocks*. Berlin Heidelberg New York Tokyo: Springer-Verlag. Retrieved from http://www.springer.com/gp/book/9783540513414

Hacker, B., Luffi, P., Lutkov, V., Minaev, V., Ratschbacher, L., Plank, T., et al. (2005). Near-ultrahigh pressure processing of continental crust: Miocene crustal xenoliths from the Pamir. *Journal of Petrology*, *46*(8), 1661–1687. https://doi.org/10.1093/petrology/egi030

Hacker, B. R., Gnos, E., Ratschbacher, L., Grove, M., McWilliams, M., Sobolev, S. V., et al. (2000). Hot and dry deep crustal xenoliths from Tibet. *Science*, *287*(5462), 2463–2466. https://doi.org/10.1126/science.287.5462.2463

Hacker, B. R., Lothar, R., Daniel, R., Stearns, M. A., Nicole, M., Konstanze, S., et al. (2017). Building the Pamir-Tibet Plateau—Crustal stacking, extensional collapse, and lateral extrusion in the Pamir: 3. Thermobarometry and petrochronology of deep Asian crust. *Tectonics*, *36*, 1743–1766. https://doi.org/10.1002/2017TC004488

Iverson, R. M. (1997). The physics of debris flows. *Reviews of Geophysics*, *35*(3), 245–296. https://doi.org/10.1029/97RG00426

Jia, C. (1997). *Structural geology and petroleum potential in the Tarim Basin* (Vol. 1–433). Beijing: Pet. Ind. Press House.

Jiang, Y. H., Liu, Z., Jia, R. Y., Liao, S. Y., Zhou, Q., & Zhao, P. (2012). Miocene potassic granite-syenite association in western Tibetan Plateau: Implications for shoshonitic and high Ba-Sr granite genesis. *Lithos*, *134-135*, 146–162. https://doi.org/10.1016/j.lithos.2011.12.012

Johnson, J. B., & Palma, J. L. (2015). Lahar infrasound associated with Volcán Villarrica's 3 March 2015 eruption. *Geophysical Research Letters*, *42*, 6324–6331. https://doi.org/10.1002/2015GL065024

Jourdan, F., Frew, A., Joly, A., Mayers, C., & Evans, N. J. (2014). WA1ms: A ~2.61Ga muscovite standard for ^{40}Ar/^{39}Ar dating. *Geochimica et Cosmochimica Acta*, *141*, 113–126. https://doi.org/10.1016/j.gca.2014.06.010

Jourdan, F., & Renne, P. R. (2007). Age calibration of the Fish Canyon sanidine ^{40}Ar/^{39}Ar dating standard using primary K–Ar standards. *Geochimica et Cosmochimica Acta*, *71*(2), 387–402. https://doi.org/10.1016/j.gca.2006.09.002

Ke, S., Mo, X., Luo, Z., Liang, T., Zhan, H., Li, L., & Li, W. (2006). Petrogenesis and geochemistry of Cenozoic Taxkorgan alkalic complex and its geological significance. *Acta Petrologica Sinica*, *22*(4), 905–915.

Kooijman, E., Smit, M. A., Ratschbacher, L., & Kylander-Clark, A. R. C. (2017). A view into crustal evolution at mantle depths. *Earth and Planetary Science Letters*, *465*, 59–69. https://doi.org/10.1016/j.epsl.2017.02.032

Koppers, A. A. P. (2002). ArArCALC—Software for ^{40}Ar/^{39}Ar age calculations. *Computers & Geosciences*, *28*(5), 605–619. https://doi.org/10.1016/S0098-3004(01)00095-4

Kufner, S.-K., Schurr, B., Sippl, C., Yuan, X., Ratschbacher, L., Akbar, A., et al. (2016). Deep India meets deep Asia: Lithospheric indentation, delamination and break-off under Pamir and Hindu Kush (Central Asia). *Earth and Planetary Science Letters*, *435*, 171–184. https://doi.org/10.1016/j.epsl.2015.11.046

Lukens, C. E., Carrapa, B., Singer, B. S., & Gehrels, G. (2012). Miocene exhumation of the Pamir revealed by detrital geothermochronology of Tajik rivers. *Tectonics*, *31*, TC2014. https://doi.org/10.1029/2011TC003040

Lutkov, B. S., Babaev, A. M., Dmitriev, E. A., Mogarovskii, V. V., Minaev, V. E., Lutkov, B. S., et al. (2005). The composition, genesis, and mantle xenoliths of the Late Miocene fergusite-carbonatite-syenite series of the Pamir: The problem of superthick crust formation in mobile belts. *Russian Journal of Earth Sciences*, *7*(1), 35–50. https://doi.org/10.2205/2005ES000170

Mattern, F., & Schneider, W. (2000). Suturing of the proto- and paleo-Tethys oceans in the western Kunlun (Xinjiang, China). *Journal of Asian Earth Sciences*, *18*(6), 637–650. https://doi.org/10.1016/S1367-9120(00)00011-0

McDonough, W. F., Sun, S.-S., Ringwood, A. E., Jagoutz, E., & Hofmann, A. W. (1992). Potassium, rubidium, and cesium in the Earth and Moon and the evolution of the mantle of the Earth. *Geochimica et Cosmochimica Acta*, *56*(3), 1001–1012. https://doi.org/10.1016/0016-7037(92)90043-I

McDougall, I., & Harrison, T. M. (1999). *Geochronology and thermochronology by the $^{40}Ar/^{39}Ar$ method*. Cambridge: Oxford University Press.

McPhie, J., Doyle, M., Allen, R. L., & Allen, R. (1993). *Volcanic textures: A guide to the interpretation of textures in volcanic rocks*. Centre for Ore Deposit and Exploration Studies. Hobart: University of Tasmania.

Pan, Y. (1996). *Geological evolution of the Karakorum and Kunlun Mountains*. Beijing: Seismological Press.

Phillips, D., & Matchan, E. L. (2013). Ultra-high precision $^{40}Ar/^{39}Ar$ ages for Fish Canyon Tuff and Alder Creek rhyolite sanidine: New dating standards required? *Geochimica et Cosmochimica Acta*, *121*, 229–239. https://doi.org/10.1016/j.gca.2013.07.003

Pierson, T. C. (1995). Flow characteristics of large eruption-triggered debris flows at snow-clad volcanoes: Constraints for debris-flow models. *Journal of Volcanology and Geothermal Research*, *66*(1-4), 283–294. https://doi.org/10.1016/0377-0273(94)00070-W

Putnis, A., Putnis, C., & Giampaolo, C. (1994). The microtexture of analcime phenocrysts in igneous rocks. *European Journal of Mineralogy*, *6*(5), 627–632. https://doi.org/10.1127/ejm/6/5/0627

Renne, P. R., Balco, G., Ludwig, K. R., Mundil, R., & Min, K. (2011). Response to the comment by W. H. Schwarz et al. on "Joint determination of 40K decay constants and $^{40}Ar*/^{40}K$ for the Fish Canyon sanidine standard, and improved accuracy for $^{40}Ar/^{39}Ar$ geochronology" by PR Renne et al. (2010). *Geochimica et Cosmochimica Acta*, *75*(17), 5097–5100. https://doi.org/10.1016/j.gca.2011.06.021

Rittner, M., Vermeesch, P., Carter, A., Bird, A., Stevens, T., Garzanti, E., et al. (2016). The provenance of Taklamakan desert sand. *Earth and Planetary Science Letters*, *437*, 127–137. https://doi.org/10.1016/j.epsl.2015.12.036

Robinson, A. C., Ducea, M., & Lapen, T. J. (2012). Detrital zircon and isotopic constraints on the crustal architecture and tectonic evolution of the northeastern Pamir. *Tectonics*, *31*, TC2016. https://doi.org/10.1029/2011TC003013

Robinson, A. C., Yin, A., Manning, C. E., Harrison, T. M., Zhang, S.-H., & Wang, X.-F. (2004). Tectonic evolution of the northeastern Pamir: Constraints from the northern portion of the Cenozoic Kongur Shan extensional system, western China. *Geological Society of America Bulletin*, *116*(7), 953–973. https://doi.org/10.1130/B25375.1

Robinson, A. C., Yin, A., Manning, C. E., Harrison, T. M., Zhang, S.-H., & Wang, X.-F. (2007). Cenozoic evolution of the eastern Pamir: Implications for strain-accommodation mechanisms at the western end of the Himalayan-Tibetan orogen. *Geological Society of America Bulletin*, *119*(7–8), 882–896. https://doi.org/10.1130/B25981.1

Rutte, D., Ratschbacher, L., Khan, J., Stübner, K., Hacker, B. R., Stearns, M. A., et al. (2017). Building the Pamir-Tibetan Plateau—Crustal stacking, extensional collapse, and lateral extrusion in the Central Pamir: 2. Timing and rates. *Tectonics*, *36*, 385–419. https://doi.org/10.1002/2016TC004294

Rutte, D., Ratschbacher, L., Schneider, S., Stübner, K., Stearns, M. A., Gulzar, M. A., & Hacker, B. R. (2017). Building the Pamir-Tibetan Plateau—Crustal stacking, extensional collapse, and lateral extrusion in the Central Pamir: 1. Geometry and kinematics. *Tectonics*, *36*, 342–384. https://doi.org/10.1002/2016TC004293

Schmidt, J., Hacker, B. R., Ratschbacher, L., Stübner, K., Stearns, M., Kylander-Clark, A., et al. (2011). Cenozoic deep crust in the Pamir. *Earth and Planetary Science Letters*, *312*(3–4), 411–421. https://doi.org/10.1016/j.epsl.2011.10.034

Schurr, B., Ratschbacher, L., Sippl, C., Gloaguen, R., Yuan, X., & Mechie, J. (2014). Seismotectonics of the Pamir. *Tectonics*, *33*, 1501–1518. https://doi.org/10.1002/2014TC003576

Schwab, M., Ratschbacher, L., Siebel, W., McWilliams, M., Minaev, V., Lutkov, V., et al. (2004). Assembly of the Pamirs: Age and origin of magmatic belts from the southern Tien Shan to the southern Pamirs and their relation to Tibet. *Tectonics*, *23*, TC4002. https://doi.org/10.1029/2003TC001583

Scott, K. M. (1988). Origins, behavior, and sedimentology of lahars and lahar-runout flows in the Toutle-Cowlitz River system (USGS Numbered Series No. 1447- A). Retrieved from http://pubs.er.usgs.gov/publication/pp1447A

Scott, K. M., Macias, J. L., Naranjo, J. A., Rodriguez, S., & McGeehin, J. P. (2001). Catastrophic debris flows transformed from landslides in volcanic terrains: mobility, hazard assessment and mitigation strategies (USGS Numbered Series No. 1630). Retrieved from http://pubs.er.usgs.gov/publication/pp1630

Shaffer, M., Hacker, B. R., Ratschbacher, L., & Kylander-Clark Andrew, R. C. (2017). Foundering triggered by the collision of India and Asia captured in xenoliths. *Tectonics*, *36*, 1913–1933. https://doi.org/10.1002/2017TC004704

Siebert, L., Glicken, H., & Ui, T. (1987). Volcanic hazards from Bezymianny- and Bandai-type eruptions. *Bulletin of Volcanology*, *49*(1), 435–459. https://doi.org/10.1007/BF01046635

Sippl, C., Schurr, B., Tympel, J., Angiboust, S., Mechie, J., Yuan, X., et al. (2013). Deep burial of Asian continental crust beneath the Pamir imaged with local earthquake tomography. *Earth and Planetary Science Letters*, *384*, 165–177. https://doi.org/10.1016/j.epsl.2013.10.013

Smith, G. A. (1986). Coarse-grained nonmarine volcaniclastic sediment: Terminology and depositional process. *Geological Society of America Bulletin*, *97*(1), 1–10. https://doi.org/10.1130/0016-7606(1986)97<1:CNVSTA>2.0.CO;2

Smith, Gary A., & Lowe, D. R. (1991). Lahars: Volcano hydrologic events and deposition in the debris flow—Hyperconcentrated flow continuum. Retrieved from http://archives.datapages.com/data/sepm_sp/SP45/Lahars_Volcano_Hydrologic_Events.html

Smith, G. A. (1991). Lahars: Volcano-hydrologic events and deposition in the debris flow-hyperconcentrated flow continuum. In *Sedimentation in volcanic settings* (Vol. 45, pp. 59–70). Tulsa: Special Publications of SEPM. Retrieved from http://sp.sepmonline.org/content/sepspsei/1/SEC6.abstract

Sobel, E. R., Chen, J., Schoenbohm, L. M., Thiede, R., Stockli, D. F., Sudo, M., & Strecker, M. R. (2013). Oceanic-style subduction controls late Cenozoic deformation of the Northern Pamir orogen. *Earth and Planetary Science Letters*, *363*, 204–218. https://doi.org/10.1016/j.epsl.2012.12.009

Sobel, E. R., & Dumitru, T. A. (1997). Thrusting and exhumation around the margins of the western Tarim basin during the India-Asia collision. *Journal of Geophysical Research*, *102*(B3), 5043–5063. https://doi.org/10.1029/96JB03267

Sobel, E. R., Schoenbohm, L. M., Chen, J., Thiede, R., Stockli, D. F., Sudo, M., & Strecker, M. R. (2011). Late Miocene-Pliocene deceleration of dextral slip between Pamir and Tarim: Implications for Pamir orogenesis. *Earth and Planetary Science Letters*, *304*(3–4), 369–378. https://doi.org/10.1016/j.epsl.2011.02.012

Stearns, M. A., Hacker, B. R., Ratschbacher, L., Lee, J., Cottle, J. M., & Kylander-Clark, A. (2013). Synchronous Oligocene–Miocene metamorphism of the Pamir and the north Himalaya driven by plate-scale dynamics. *Geology*, *41*(10), 1071–1074. https://doi.org/10.1130/G34451.1

Stübner, K., Ratschbacher, L., Rutte, D., Stanek, K., Minaev, V., Wiesinger, M., et al. (2013). The giant Shakhdara migmatitic gneiss dome, Pamir, India-Asia collision zone: 1. Geometry and kinematics. *Tectonics*, *32*, 948–979. https://doi.org/10.1002/tect.20057

Sun, J., Alloway, B., Fang, X., & Windley, B. F. (2015). Refuting the evidence for an earlier birth of the Taklimakan Desert. *Proceedings of the National Academy of Sciences*, *112*(41), E5556–E5557. https://doi.org/10.1073/pnas.1517525112

Thiede, R. C., Sobel, E. R., Chen, J., Schoenbohm, L. M., Stockli, D. F., Sudo, M., & Strecker, M. R. (2013). Late Cenozoic extension and crustal doming in the India-Eurasia collision zone: New thermochronologic constraints from the NE Chinese Pamir. *Tectonics*, *32*, 763–779. https://doi.org/10.1002/tect.20050

Thomas, J.-C., Chauvin, A., Gapais, D., Bazhenov, M. L., Perroud, H., Cobbold, P. R., & Burtman, V. S. (1994). Paleomagnetic evidence for Cenozoic block rotations in the Tadjik depression (Central Asia). *Journal of Geophysical Research*, *99*(B8), 15,141–15,160. https://doi.org/10.1029/94JB00901

Tost, M., Cronin, S. J., & Procter, J. N. (2014). Transport and emplacement mechanisms of channelised long-runout debris avalanches, Ruapehu volcano, New Zealand. *Bulletin of Volcanology*, *76*(12), 881. https://doi.org/10.1007/s00445-014-0881-z

Ui, T., Takarada, S., & Yoshimoto, M. (2000). Debris avalanches. In *Encyclopedia of volcanoes* (pp. 617–626). San Diego: Academic Press.

Umbal, J. V., & Rodolfo, K. S. (1996). The 1991 lahars of southwestern Mount Pinatubo and evolution of the lahar-dammed Mapanuepe Lake. Fire and Mud: Eruptions and Lahars of Mount Pinatubo, Philippines: Quezon, Philippines, 951–970.

Vallance, J. W. (1999). Postglacial lahars and potential hazards in the White Salmon River system on the southwest flank of Mount Adams, Washington (USGS Numbered Series No. 2161). U.S. Dept. of the Interior, U.S. Geological Survey; Information Services [distributor],. Retrieved from http://pubs.er.usgs.gov/publication/b2161

Vallance, J. W., & Scott, K. M. (1997). The Osceola mudflow from Mount Rainier: Sedimentology and hazard implications of a huge clay-rich debris flow. *Geological Society of America Bulletin*, *109*(2), 143–163. https://doi.org/10.1130/0016-7606(1997)109<0143:TOMFMR>2.3.CO;2

Waitt, R. B. (2007). Primary volcaniclastic rocks: Comment and reply comment. *Geology*, *35*(1), e141–e141. https://doi.org/10.1130/G23685C.1

Wei, H. H., Meng, Q. R., Ding, L., & Li, Z. Y. (2013). Tertiary evolution of the western Tarim basin, northwest China: A tectono-sedimentary response to northward indentation of the Pamir salient. *Tectonics*, *32*, 558–575. https://doi.org/10.1002/Tect.20046

White, J. D. L., & Houghton, B. F. (2007). Primary volcaniclastic rocks: Comment and reply reply. *Geology*, *35*(1), e142–e142. https://doi.org/10.1130/G23985Y.1

Xiao, W., Han, F., Windley, B. F., Yuan, C., Zhou, H., & Li, J. (2003). Multiple accretionary orogenesis and episodic growth of continents: Insights from the western Kunlun range, Central Asia. *International Geology Review*, *45*(4), 303–328. https://doi.org/10.2747/0020-6814.45.4.303

Xiao, W. J., Windley, B. F., Chen, H. L., Zhang, G. C., & Li, J. L. (2002). Carboniferous-Triassic subduction and accretion in the western Kunlun, China: Implications for the collisional and accretionary tectonics of the northern Tibetan Plateau. *Geology*, *30*(4), 295–298. https://doi.org/10.1130/0091-7613(2002)030<0295:CTSAAI>2.0.CO;2

Yarnold, J. C., & Lombard, J. P. (1989). A facies model for large rock-avalanche deposits formed in dry climates, 9–31.

Yin, A., Rumelhart, P. E., Butler, R., Cowgill, E., Harrison, T. M., Foster, D. A., et al. (2002). Tectonic history of the Altyn Tagh fault system in northern Tibet inferred from Cenozoic sedimentation. *Geological Society of America Bulletin*, *114*(10), 1257–1295. https://doi.org/10.1130/0016-7606(2002)114<1257:THOTAT>2.0.CO;2

Zheng, H., Tada, R., Jia, J., Lawrence, C., & Wang, K. (2010). Cenozoic sediments in the southern Tarim Basin: Implications for the uplift of northern Tibet and evolution of the Taklimakan Desert. In P. Clift, R. Tada, & H. Zheng (Eds.), *Monsoon evolution and tectonics—Climate linkage in Asia* (Vol. 342, pp. 67–78). London: Geol. Soc. London Spec. Publ.

Zheng, H., Wei, X., Tada, R., Clift, P. D., Wang, B., Jourdan, F., et al. (2015a). Late Oligocene–early Miocene birth of the Taklimakan Desert. *Proceedings of the National Academy of Sciences*, *112*(25), 7662–7667. https://doi.org/10.1073/pnas.1424487112

Zheng, H., Wei, X., Tada, R., Clift, P. D., Wang, B., Jourdan, F., et al. (2015b). Reply to Sun et al.: Confirming the evidence for Late Oligocene–Early Miocene birth of the Taklimakan Desert. *Proceedings of the National Academy of Sciences*, *112*(41), E5558–E5559. https://doi.org/10.1073/pnas.1517735112

Zheng, H. B., Huang, X. T., & Butcher, K. (2006). Lithostratigraphy, petrography and facies analysis of the Late Cenozoic sediments in the foreland basin of the West Kunlun. *Palaeogeography Palaeoclimatology Palaeoecology*, *241*(1), 61–78. https://doi.org/10.1016/j.palaeo.2006.06.015